Monthly Notices
of the
ROYAL ASTRONOMICAL SOCIETY

Mon. Not. R. Astron. Soc. **422,** 44–69 (2012) doi:10.1111/j.1365-2966.2012.20443.x

The X-ray cluster survey with *eROSITA*: forecasts for cosmology, cluster physics and primordial non-Gaussianity

Annalisa Pillepich,[1,2⋆] Cristiano Porciani[3] and Thomas H. Reiprich[3]

[1]*Institute for Astronomy, ETH Zurich, 8093 Zurich, Switzerland*
[2]*UCO/Lick Observatory, University of California, Santa Cruz, CA 95064, USA*
[3]*Argelander-Institut für Astronomie, Auf dem Hügel 71, D-53121 Bonn, Germany*

Accepted 2011 December 22. Received 2011 December 21; in original form 2011 September 15

ABSTRACT

Starting in late 2013, the *eROSITA* telescope will survey the X-ray sky with unprecedented sensitivity. Assuming a detection limit of 50 photons in the (0.5–2.0) keV energy band with a typical exposure time of 1.6 ks, we predict that *eROSITA* will detect $\sim 9.3 \times 10^4$ clusters of galaxies more massive than $5 \times 10^{13}\, h^{-1}\, \mathrm{M}_\odot$, with the currently planned all-sky survey. Their median redshift will be $z \simeq 0.35$. We perform a Fisher-matrix analysis to forecast the constraining power of *eROSITA* on the Λ cold dark matter (ΛCDM) cosmology and, simultaneously, on the X-ray scaling relations for galaxy clusters. Special attention is devoted to the possibility of detecting primordial non-Gaussianity. We consider two experimental probes: the number counts and the angular clustering of a photon-count limited sample of clusters. We discuss how the cluster sample should be split to optimize the analysis and we show that redshift information of the individual clusters is vital to break the strong degeneracies among the model parameters. For example, performing a 'tomographic' analysis based on photometric-redshift estimates and combining one- and two-point statistics will give marginal 1σ errors of $\Delta\sigma_8 \simeq 0.036$ and $\Delta\Omega_\mathrm{m} \simeq 0.012$ without priors, and improve the current estimates on the slope of the luminosity–mass relation by a factor of 3. Regarding primordial non-Gaussianity, *eROSITA* clusters alone will give $\Delta f_\mathrm{NL} \simeq 9$, 36 and 144 for the local, orthogonal and equilateral model, respectively. Measuring redshifts with spectroscopic accuracy would further tighten the constraints by nearly 40 per cent (barring f_NL which displays smaller improvements). Finally, combining *eROSITA* data with the analysis of temperature anisotropies in the cosmic microwave background by the *Planck* satellite should give sensational constraints on both the cosmology and the properties of the intracluster medium.

Key words: galaxies: clusters: general – cosmological parameters – early Universe – large-scale structure of Universe – X-rays: galaxies: clusters.

1 INTRODUCTION

eROSITA[1] (Predehl 2006; Predehl et al. 2010) is the primary science instrument onboard the *Spectrum-Roentgen-Gamma* (*SRG*) satellite,[2] a fully funded mission with a currently planned launch in late 2013. *eROSITA* will perform an X-ray all-sky survey with a sensitivity ∼30 times better than *ROSAT*. Assuming a detection limit of 50 photons in the (0.5–2.0) keV energy band and with an average exposure time of ∼1.6 ks, we expect that *eROSITA* will be able to detect *all* clusters of galaxies in the observable Universe with masses higher than $\sim 3 \times 10^{14}\, h^{-1}\, \mathrm{M}_\odot$. This makes it an ideal probe of cosmology.

The evolution in the number density of massive galaxy clusters as well as their clustering properties strongly depends on the cosmological parameters. Cluster number counts trace the normalization and the growth of linear density perturbations (e.g. Allen, Evrard & Mantz 2011). The mass function of clusters detected in X-rays by *ROSAT* and re-observed with *Chandra* has been recently used to delve into the mystery of cosmic acceleration and thus constrain the equation-of-state parameter of dark energy (Vikhlinin et al. 2009b; Mantz et al. 2010b). These studies are based on samples containing a few tens of galaxy clusters.

The advent of *eROSITA* will produce cluster catalogues with $\sim 10^5$ objects. Photometric redshifts of the X-ray-detected clusters

⋆E-mail: annalisa.pillepich@ucolick.org
[1] Extended ROentgen Survey with an Imaging Telescope Array, http://www.mpe.mpg.de/erosita/.
[2] http://hea.iki.rssi.ru/SRG/en/index.php

will become available thanks to a series of complementary multi-band optical surveys (e.g. PanSTARRS,[3] DES,[4] and LSST[5]), while planned massive spectroscopic surveys are designed with *eROSITA* follow-up as science driver, e.g. 4MOST.[6] All this will vastly improve upon current cosmological constraints. *eROSITA* will likely be the first stage IV dark-energy experiment (as described in the US Dark Energy Task Force report; Albrecht et al. 2006) to be realized.

At the same time, better data will allow us to relax some model assumptions. An interesting example is given by the statistical properties of the primordial density perturbations that seeded structure formation in the Universe. They are often modelled with a Gaussian random field. In fact, the simplest inflationary models predict negligible – i.e. well below the current detection limit – levels of primordial non-Gaussianity. Nevertheless, other theories for the generation of the primordial density fluctuations (both inflationary and not) can produce measurable levels of primordial non-Gaussianity, e.g. multiple-scalar-field scenarios, curvaton models, ghost inflation and topological defects (see Bartolo et al. 2004; Chen 2010, and references therein for a complete review). Quantifying the primordial non-Gaussian signal has thus emerged as one of the most powerful tools to test and discriminate among competing scenarios for the generation of primordial density fluctuations.

Primordial non-Gaussianity is expected to leave imprints on the large-scale structure of the evolved universe, ranging from the abundance of collapsed massive objects to their spatial clustering properties (see Desjacques & Seljak 2010, and references therein for an updated review). Clusters of galaxies as tracers of the underlying dark matter (DM) haloes are thus an optimal target for the search of primordial non-Gaussianity.

Regrettably, theoretical models provide robust predictions for the halo abundance and clustering only in terms of DM masses. Therefore, some knowledge of the relation between cluster observables and the corresponding halo masses is required to constrain cosmological parameters. In X-ray astronomy, cluster masses can be determined exploiting a series of scaling relations (luminosity–mass, temperature–mass, gas mass–total mass), whose shape and magnitude can be inferred by dedicated observations or by invoking assumptions about the properties of the intracluster medium (ICM). Once the functional form of these relations is known, large cluster samples can be used to derive self-consistent constraints on cosmological and scaling-relation parameters from the same data set (the so-called self-calibration approach; Hu 2003; Majumdar & Mohr 2003). This should also provide some insight into the gas physics of the ICM. Note, however, that dedicated observations will be anyway necessary to test the range of validity of the assumed scaling relations and provide an independent test of the retrieved parameters.

The goal of this paper is to assess the power of *eROSITA* in the simultaneous determination of cosmological and scaling-relation parameters, also accounting for primordial non-Gaussianity. Forecasts are made using the Fisher information matrix for the measurements of the abundance and two-point spatial clustering of X-ray-selected clusters. A series of papers have recently addressed similar topics. Oguri (2009) and Cunha, Huterer & Doré (2010) discussed optical surveys as the HSC,[7] DES and LSST. Similarly, Sartoris et al. (2010) focused on the envisaged X-ray satellite *WFXT*.[8] More qualitative analyses have been carried out by Fedeli, Moscardini & Matarrese (2009), Roncarelli et al. (2010) and Fedeli et al. (2011) for the *eROSITA*, the South-Pole-Telescope and the Euclid surveys, yet not providing detailed forecasts, or with no assessment of the effect of the uncertainties in the scaling relations, or only considering a small subset of cosmological parameters. Our work differentiates from the previous ones in the sense that it is meticulously tailored around *eROSITA* and the actual way observations will be taken. Galaxy-cluster number counts and power spectra are calculated in terms of the raw photon counts that will be detected at the telescope. This is done by adopting observationally motivated X-ray scaling relations, taking into account the spectral energy distribution of the ICM emission, the photoelectric absorption suffered by the photons along the line of sight and the expected telescope response.

The plan of the paper is as follows. In Section 2, we explain how we compute the expected abundances and projected angular clustering of DM haloes in the presence of primordial non-Gaussianity and in Section 3 we define our fiducial model. In Section 4, we focus on the transformation between actual halo masses and observed photon counts. The *eROSITA* cluster survey is described in detail in Section 5, while the experiments we consider are discussed in Section 6. In Section 7, we describe how we compute the Fisher information matrix while, in Section 8, we derive the constraints on the cosmological and scaling-relation parameters for an all-sky survey with *eROSITA*, giving special attention to the primordial non-Gaussianity parameter of the local type, $f_{\rm NL}^{\rm local}$. We consider two experiments: the measurement of cluster abundances and of the corresponding angular power spectrum. For both probes, we distinguish the cases in which redshift information on the individual clusters is available or not. Eventually we combine the different *eROSITA* measurements and also discuss how the model constraints are consolidated by using the (currently forecasted) results of the *Planck* satellite as a prior probability distribution. Table 3 summarizes our main findings. We investigate the effects of modifying the survey strategies and changing the observational cuts in Section 9, while in Section 10 we extend our analysis to other interesting models of primordial non-Gaussianity, complementary to the local type: the so-called orthogonal and equilateral shapes. A thorough discussion of the assumptions in our analysis is presented in Section 11, where we quantify the effects of changing the fiducial model and adding extra parameters. Our conclusions are summarized in Section 12.

2 MASS FUNCTION AND BIAS OF DARK MATTER HALOES

2.1 Halo definition

The densest regions of the cosmic matter distribution are commonly dubbed 'DM haloes'. Their outer boundaries (and thus their masses) are somewhat arbitrary depending on the adopted definition. In numerical simulations, haloes are most commonly identified using either the friends-of-friends (FOF) or the spherical overdensity (SO) algorithms (Einasto et al. 1984; Davis et al. 1985). While the FOF method approximately tracks isodensity contours (Efstathiou et al. 1985; More et al. 2011), the SO one fixes the mean density of the structure within a sphere grown around the halo centre. We define M_Δ to be the mass enclosed in a sphere whose mean density is

[3] Panoramic Survey Telescope and Rapid Response Systems.
[4] Dark Energy Survey.
[5] Large Synoptic Survey Telescope.
[6] 4-m Multi-Object Spectroscopic Telescope for ESO.
[7] Hyper Suprime-Cam on Subaru telescope.
[8] Wide Field X-ray Telescope.

Δ times the critical density of the universe at the time the halo is considered:

$$M_\Delta = \frac{4}{3}\pi(\Delta\,\rho_{\rm crit})R_\Delta^3. \quad (1)$$

This definition is widespread among observers and slightly differs from what is commonly adopted by the numerical community where the background density $\bar{\rho}_{\rm m}$ is used instead of the critical one. Thus, for a given population of SO haloes, the values that the parameter Δ assumes in the two approaches differ by a factor $\Omega_{\rm m}(z) = \bar{\rho}_{\rm m}(z)/\rho_{\rm crit}(z)$.

From an observational point of view, it is standard to define cluster masses adopting the SO algorithm. In fact, for X-ray observations of galaxy clusters, better measurements of the gas mass and temperature can be achieved in regions with high-density contrast where structures are much brighter and relatively relaxed with respect to the outer regions (and also the assumption of hydrostatic equilibrium is more accurate). On the other hand, observational results should be compared with numerical simulations where the finite resolution and force softening might create problems for very high values of Δ. For these reasons, the best compromise is to define the DM haloes in terms of M_{500}.

2.2 Halo mass function

The halo mass function, $\mathrm{d}n/\mathrm{d}M(M, z)$, gives the halo abundance per unit volume and per unit mass as a function of redshift. It is conveniently described in terms of the function f, defined as

$$\frac{\mathrm{d}n}{\mathrm{d}M}(M, z) = f(\sigma, z)\,\frac{\bar{\rho}_{\rm m,0}}{M}\,\frac{\mathrm{d}\,\ln[\sigma^{-1}(M, z)]}{\mathrm{d}M}\,, \quad (2)$$

where $\bar{\rho}_{\rm m,0}$ denotes the mean background matter density today, and $\sigma^2(M, z)$ is the variance of the smoothed linear density field, $\langle\delta_M^2(z)\rangle$:

$$\sigma^2(M, z) = \frac{1}{2\pi^2}\int_0^\infty k^2\,P_{\rm lin}(k, z)\,W^2(k, M)\,\mathrm{d}k, \quad (3)$$

with $P_{\rm lin}(k, z)$ the corresponding power spectrum and $W(k, M)$ a window function with mass resolution M; here we use a top-hat filter in real space, which in Fourier space reads

$$W(k, M) = 3\,\frac{\sin(x) - x\cos(x)}{x^3}, \quad (4)$$

where $x \equiv kR$ and $M = (4/3)\pi\bar{\rho}_{\rm m}R^3$. The function f is calibrated against high-resolution numerical simulations and different parametrization are available in the literature. Following Tinker et al. (2008), we assume that the function f weakly depends on z and Δ_b, where Δ_b defines the mean overdensity of SO haloes as in equation (1) but with respect to the evolving mean background density of the universe. For Gaussian initial conditions, we thus write

$$f_{\rm T}(\sigma, z, \Delta_b) = A\left[\left(\frac{\sigma}{b}\right)^{-a} + 1\right]\exp\left(-\frac{c}{\sigma^2}\right), \quad (5)$$

with

$$\begin{aligned} A(\Delta_b, z) &= A_0^{\rm TMF}(\Delta_b)(1+z)^{-A_z^{\rm TMF}},\\ a(\Delta_b, z) &= a_0^{\rm TMF}(\Delta_b)(1+z)^{-a_z^{\rm TMF}},\\ b(\Delta_b, z) &= b_0^{\rm TMF}(\Delta_b)(1+z)^{-\alpha},\\ c(\Delta_b, z) &= c_0^{\rm TMF}(\Delta_b),\\ \log_{10}(\alpha(\Delta_b)) &= -\left[\frac{0.75}{\log_{10}(\Delta_b/75)}\right]^{1.2}, \end{aligned} \quad (6)$$

where $A_z^{\rm TMF} = 0.14$ and $a_z^{\rm TMF} = 0.06$. The zero subscripts indicate the values of the parameters obtained at $z = 0$ and listed in table 2 of Tinker et al. (2008). Note that because of the different definition of SO halo masses, an interpolation of the best-fitting parameters of table 2 in Tinker et al. (2008) is required to compute these coefficients. For Gaussian initial conditions, this formula for the DM halo mass function reproduces to 5 per cent level of accuracy the abundance of SO haloes in N-body simulations for different choices of the standard cosmological parameters and for a wide range of masses and redshifts which encompasses what is probed by *eROSITA*.

2.3 Non-Gaussian corrections

We consider here extensions to the standard cosmological model where the primordial curvature perturbations (more precisely the Bardeen's potential) that generate the large-scale structure are not Gaussian. In the synchronous gauge and for sub-horizon perturbations in the mass density (or in the gravitational potential), these models are characterized by a non-vanishing bispectrum, $B(k_1, k_2, k_3) \neq 0$. The functional form of the bispectrum with respect to the triplet of wavenumbers $\boldsymbol{K} = (k_1, k_2, k_3)$ describes the 'shape' of primordial non-Gaussianity while its overall amplitude (at fixed $\boldsymbol{K}$) defines the 'strength' of the non-Gaussian signal. The latter is generally quantified in terms of the non-linearity parameter $f_{\rm NL}^i$, where the index i refers to a particular non-Gaussian shape. As a reference case, we first focus on the 'local' model for primordial non-Gaussianity, where the linear gravitational potential can be written as

$$\phi(\boldsymbol{x}) = g(\boldsymbol{x}) + f_{\rm NL}^{\rm local}[g^2(\boldsymbol{x}) - \sigma_g^2] + \cdots, \quad (7)$$

where g is a Gaussian random field with zero mean and variance σ_g^2. In this case, the bispectrum of linear density perturbations reads $B(k_1, k_2, k_3) \simeq 2\,f_{\rm NL}^{\rm local}\,[P_{\rm lin}(k_1)\,P_{\rm lin}(k_2) + \ 2\ \text{perms.}]$. Note that we normalize $f_{\rm NL}^{\rm local}$ by imposing the relation (7) at very high redshift which sometimes is referred to as the cosmic microwave background (CMB) normalization. We postpone to Section 10 the extension of our analysis to other non-Gaussian models, such as the equilateral and orthogonal shapes.

In general, for non-Gaussian initial conditions, we compute the halo mass function through a multiplicative correction to the Gaussian one:

$$\left(\frac{\mathrm{d}n}{\mathrm{d}M}\right)_{\rm NG} = \left(\frac{\mathrm{d}n}{\mathrm{d}M}\right)_{T, M_{500}} R_{\rm NG}(M, z, f_{\rm NL}), \quad (8)$$

[here the subscript T, M_{500} refers to the fact we use equation (5) and $\Delta = 500$]. Among the possible choices for the non-Gaussian correction $R_{\rm NG}(M, z, f_{\rm NL}^{\rm local})$, we adopt the prescription by LoVerde et al. (2008), which is in rather good agreement with numerical simulations (Giannantonio & Porciani 2010; Pillepich, Porciani & Hahn 2010):

$$R_{\rm NG}(M, z, f_{\rm NL}^{\rm local}) = 1 + \frac{1}{6}\frac{\sigma^2}{\delta_{\rm c}}\left[S_3\left(\frac{\delta_{\rm c}^4}{\sigma^4} - 2\frac{\delta_{\rm c}^2}{\sigma^2} - 1\right) + \frac{\mathrm{d}S_3}{\mathrm{d}\ln\sigma}\left(\frac{\delta_{\rm c}^2}{\sigma^2} - 1\right)\right]. \quad (9)$$

Here $\delta_{\rm c}$ is the critical density contrast for halo collapse fixed to 1.686 for SO haloes (Desjacques & Seljak 2010), while S_3 denotes the standardized third central moment (skewness) of the smoothed

density field, namely $S_3 = \langle \delta_M^3 \rangle / \sigma^4$:

$$S_3\sigma^4 = \frac{f_{\rm NL}^{\rm local}}{(2\pi^2)^2} \int {\rm d}k_1 k_1^2\ W(k_1, M)\ P_{\rm lin}(k_1) \int {\rm d}k_2 k_2^2\ W(k_2, M)\ P_{\rm lin}(k_2) \int_{-1}^{1} {\rm d}\mu\ W(k_{12}, M) \left[1 + 2\frac{P_{\rm lin}(k_{12})}{P_{\rm lin}(k_2)}\right], \quad (10)$$

where $k_{12}^2 = k_1^2 + k_2^2 + 2\mu k_1 k_2$.

Note that we do not use the direct fitting formulae for the $f_{\rm NL}^{\rm local}$-dependent mass function presented in Pillepich et al. (2010) as they have been obtained for FOF haloes and there is no trivial mapping between FOF and SO haloes.

2.4 Halo bias

We are not only interested in extracting cosmological information from measurements of the abundance of the X-ray clusters, but also from the angular clustering of the observed objects. From numerical and theoretical work, we know that the clustering of DM haloes in which the clusters reside is biased relative to that of the underlying mass distribution by an amount which depends on halo mass, redshift and the scale at which the clustering is considered (see e.g. Mo & White 1996; Catelan et al. 1998; Smith, Scoccimarro & Sheth 2007). In general, the bias of DM haloes can be expressed as

$$b(k, M, z) = \sqrt{\frac{P_{\rm hh}(k, M, z)}{P(k, z)}}\ , \quad (11)$$

where $P_{\rm hh}$ is the power spectrum of the halo density field and $P(k, z)$ is the matter power spectrum. Within Gaussian scenarios, the halo bias on large scales ($k \lesssim 0.05\,h\,{\rm Mpc}^{-1}$) depends on the halo mass and redshift but is independent of k (e.g. Tinker et al. 2010). We compute this linear bias using the peak-background-split model (Cole & Kaiser 1989; Mo & White 1996):

$$b_{\rm G} = 1 - \frac{1}{\delta_{\rm c}} \frac{{\rm d}\ln f}{{\rm d}\ln \sigma^{-1}}\ . \quad (12)$$

On the other hand, a strong k-dependence of the bias appears at smaller scales ($k \gtrsim 0.1\,h\,{\rm Mpc}^{-1}$), e.g. Smith et al. (2007); Manera, Sheth & Scoccimarro (2010).

Dalal et al. (2008) have shown that primordial non-Gaussianity of the local type introduces a scale-dependent correction to the large-scale bias of massive DM haloes. This is because large- and small-scale density fluctuations are not independent when $f_{\rm NL}^{\rm local} \neq 0$. We thus extend the expression for the halo bias to non-Gaussian scenarios following Giannantonio & Porciani (2010):

$$b(k, M, z) = b_{\rm G} + f_{\rm NL}^{\rm local}\ (b_{\rm G} - 1)\ \frac{\Gamma}{\alpha(k, z)}. \quad (13)$$

which is in good agreement with N-body simulations as shown by Giannantonio & Porciani (2010) and Desjacques, Seljak & Iliev (2009). In equation (13), the different factors read $\Gamma = 3\,\delta_{\rm c}\,\Omega_{\rm m}\,H_0^2/c^2$ and $\alpha(k, z) = k^2\,T(k)\,D(z)\,g(0)/g(\infty)$, where $T(k)$ is the linear matter transfer function, $D(z)$ is the linear growth factor of the density perturbations (normalized to unity today), and $g(z)$ is the growth factor of the potential perturbations. Throughout this paper, we use the linear matter transfer function $T(k)$ computed using the LINGER code by Bertschinger (2001).

3 FIDUCIAL MODEL

We consider a flat Λ cold dark matter (ΛCDM) universe characterized by five standard parameters (three for the background – $\Omega_{\rm m}$, $\Omega_{\rm b}$ and h – and two for the scalar perturbations – $n_{\rm s}$ and σ_8). On top of this we introduce the extra parameter $f_{\rm NL}^{\rm local}$. We list all the model parameters and the choice of their fiducial values in Table 1, where we distinguish among cosmological, cluster physics (see Section 4) and survey (see Section 5) parameters. We assume Gaussian perturbations as our fiducial case, i.e. $f_{\rm NL}^{\rm local} = 0$. We choose the other fiducial values by adopting the best-fitting parameters from the combination of 5-yr data from the *Wilkinson Microwave Anisotropy Probe* (*WMAP*), baryonic acoustic oscillations (BAO) and supernovae Ia (SN); see Komatsu et al. (2009).

4 FROM HALO MASS TO X-RAY PHOTON COUNTS

eROSITA will perform an X-ray all-sky survey in about 4 years starting in late 2013, from a L2 orbit. The instrument will consist of seven identical Wolter-1 mirror modules of 358 mm of diameter, each containing 54 nested mirror shells, and of a fast frame-store pn-CCD detector. This will result in a 1° field of view, an effective area of 1500 cm^2 at 1.5 keV and an averaged point spread function of 25–30 arcsec half energy width (HEW; on-axis: 15 arcsec HEW). It will operate in the broad energy range (0.5–10) keV.

In order to convert non-observable quantities such as M_{500} into the raw photons counts effectively collected in the detector (η), a series of transformations have to be considered:[9]

$$M_{500} \rightarrow [L_{\rm X}, T_{\rm X}] \rightarrow \text{photon counts} = \eta,$$

where $L_{\rm X}$ denotes the X-ray luminosity and $T_{\rm X}$ the average temperature of the intracluster gas. Consequently, the mass function in equation (2) has to be converted in a raw-count function:

$$\frac{{\rm d}n}{{\rm d}M_{500}} \rightarrow \frac{{\rm d}n}{{\rm d}\eta}.$$

In full generality, given two variables X and Y, the conversion in the differential number counts can be performed as follows:

$$\frac{{\rm d}n}{{\rm d}Y}(Y^*) = \int \frac{{\rm d}n}{{\rm d}X}(X)\ P(Y^*|X)\,{\rm d}X, \quad (14)$$

where $P(Y|X)$ denotes the conditional probability of getting Y for given X. When the scatter in the Y–X relation is negligible (i.e. the probability P is a Dirac-delta distribution), this reduces to

$$\frac{{\rm d}n}{{\rm d}Y} = \frac{{\rm d}n}{{\rm d}X}\frac{{\rm d}X}{{\rm d}Y}. \quad (15)$$

On the other hand, any function of the variable X can be written in terms of Y as follows:

$$b_Y(Y^*) = \frac{\int b(X)\ \frac{{\rm d}n}{{\rm d}X}(X)\ P(Y^*|X)\,{\rm d}X}{\int \frac{{\rm d}n}{{\rm d}X}(X)\ P(Y^*|X)\,{\rm d}X}, \quad (16)$$

which, for negligible scatter and when $Y = f(X)$, gives

$$b_Y(Y^*) = b[f^{-1}(Y^*)]. \quad (17)$$

In the following, we summarize the specific choices we adopted to express the cluster number counts and bias in terms of the photon counts.

[9] Since the conversion between the energy flux and the photon counts depends on the energy spectrum, to mimic more closely the experimental reality we prefer not to adopt a flux limit in our analysis.

Table 1. Model and survey parameters plus their fiducial values. The parameters which are allowed to vary in the Fisher-matrix analysis are typed in boldface. Note that we assume a flat cosmology where $\Omega_\Lambda = 1 - \Omega_m$ throughout the statistical analysis.

	Description	Fiducial value	Current error[a]	Reference
Cosmological parameter				
f_{NL}^{local}	**Non-linearity parameter (local)**	0	$-9 \leq f_{NL}^{local} \leq +111$	Komatsu et al. (2009)
σ_8	**Normalization of $P(k)$**	0.817	± 0.026	Komatsu et al. (2009)
Ω_m	**DM fraction**	0.279	± 0.0058	Komatsu et al. (2009)
n_s	**Spectral index**	0.96	± 0.013	Komatsu et al. (2009)
h	**Hubble constant**	0.701	± 0.013	Komatsu et al. (2009)
Ω_b	**Baryon fraction**	0.0462	± 0.0015	Komatsu et al. (2009)
Ω_Λ	Dark energy fraction	0.721	± 0.015	Komatsu et al. (2009)
w	Equation-of-state parameter (constant)	-1	$-0.14 < 1 + w < 0.12$	Komatsu et al. (2009)
X-ray cluster parameter				
α_{LM}	**LM relation: slope**	1.61	± 0.14	Vikhlinin et al. (2009a)
γ_{LM}	**LM relation: z-dependent factor**	1.85	± 0.42	Vikhlinin et al. (2009a)
β_{LM}	**LM relation: normalization**	101.483	± 0.085	Vikhlinin et al. (2009a)
σ_{LM}	**LM relation: logarithmic scatter**	0.396	± 0.039	Vikhlinin et al. (2009a)
α_{TM}	TM relation: slope	0.65	± 0.03	Vikhlinin et al. (2009a)
β_{TM}	TM relation: normalization	$3.02 \times 10^{14}\,M_\odot h^{-1}$	$\pm 0.11 \times 10^{14}$	Vikhlinin et al. (2009a)
σ_{TM}	TM relation: logarithmic scatter	0.119	0.03[b]	Kravtsov, Vikhlinin & Nagai (2006)
ρ_{LT}	LT correlation coefficient	0	–	–
Z_{ICM}	Intracluster metallicity	$0.3\,Z_\odot$	–	Anders & Grevesse (1989)
N_H	Hydrogen column density along l.o.s.	3×10^{20} atom cm^{-2}	–	Kalberla et al. (2005)
Survey parameter				
	X-ray energy band	0.5–2.0 keV	–	–
η_{min}	Minimum raw photon count	50	–	–
M_{min}	Minimum considered mass (M_{500})	$5 \times 10^{13}\,M_\odot h^{-1}$	–	–
f_{sky}	Sky coverage	$0.658 \Rightarrow 27\,145$ deg^2 [c]	–	Predehl et al. (2010)
T_{exp}	Exposure time	1.6×10^3 s (all-sky survey)	–	–

[a] *WMAP*5+BAO+SN, for the cosmology sector [68.3 per cent credibility interval (CI), with the exception of f_{NL}^{local} for which the 95.4 CI per cent is indicated].
[b] From hydrodynamical simulations, systematic error encompassing variations for different sub-populations of clusters: relaxed or unrelaxed, at low or high redshifts.
[c] All-sky survey excising $\pm 20^\circ$ around the Galactic plane.

4.1 Luminosity–mass relation

To connect cluster masses to X-ray luminosities, we refer to the L_X–M_{500} relation obtained by Vikhlinin et al. (2009a) through the observation of two sets of *Chandra* galaxy clusters with median redshifts of about 0.05 and 0.5, in the (0.5–2.0) keV rest-frame band and with L_X integrated within 2 Mpc. The luminosity–mass (LM) relation is conveniently written such that the normalization is taken at the effective mean mass, to minimize correlations among parameters:

$$\begin{aligned}\mu_L \equiv \langle \ln L_X \rangle = & \left[\beta_{LM} + 1.5(\sigma_{LM}^2 - 0.396^2)\right] \\ & + \alpha_{LM} \ln(M_{500}/3.9 \times 10^{14}\,M_\odot) \\ & + \gamma_{LM} \ln E(z) - 0.39 \ln(h/0.72) \pm \sigma_{LM}, \end{aligned} \quad (18)$$

where L_X is measured in erg s^{-1} and $E(z) = H(z)/H_0$. The slope α_{LM} reads 1.61 ± 0.14, the normalization $\left[\beta_{LM} + 1.5(\sigma_{LM}^2 - 0.396^2)\right] = 101.483 \pm 0.085$, and the redshift-dependence factor $\gamma_{LM} = 1.85 \pm 0.42$ (see Table 1). The symbol σ_{LM} on the right-hand side indicates the observed scatter in $\ln L_X$ at fixed M. The nature of such a scatter is consistent with a lognormal distribution:

$$P(\ln L_X | M) = \frac{1}{\sqrt{2\pi\sigma_{LM}^2}} \exp\left[-\frac{(\ln L_X - \mu_L)^2}{2\sigma_{LM}^2}\right], \quad (19)$$

where $\sigma_{LM} = 0.396 \pm 0.039$. This corresponds to a (symmetrized) relative error of ~ 40 per cent.

Note that since Vikhlinin et al. (2009a) determined M_{500} from the relation between Y_X (the product of T_X and gas mass) and mass, whose evolution was assumed to be self-similar based on results from numerical simulations, the redshift evolution of relation (18) has not been measured directly.

4.2 From X-ray luminosity to the number of detected photons

Given L_X in the (0.5–2.0) keV rest-frame energy band and the redshift z of the clusters, we can predict the number of photons detected by *eROSITA* in the (0.5–2.0) keV observer-frame energy band. To do this, we require further information: (i) the emitted spectrum, which depends on the temperature and metal abundance of the intracluster gas; (ii) the photoelectric absorption suffered by the X-ray photons along their way; (iii) the *eROSITA* instrumental response and effective area and (iv) the exposure time, T_{exp}.

(i) We derive the cluster average X-ray temperature using the results by Vikhlinin et al. (2009a), where the relation M_{500}–T_X is parametrized with a power law (as expected, if the temperature of the ICM scales with the depth of the gravitational potential). To measure this relation, Vikhlinin et al. (2009a) define the cluster temperature as the average spectral temperature integrated within a given radial range. Inverting the scaling relation of their table 3 with

no pre-fixed slope, we write the temperature–mass relation (TM) as

$$\mu_T \equiv \langle \ln T_{\rm X} \rangle = \alpha_{\rm TM} \ln(M_{500}/\beta_{\rm TM}) + \alpha_{\rm TM} \ln E(z) + \ln(5\,{\rm keV}) \pm \sigma_{\rm TM}, \quad (20)$$

where $T_{\rm X}$ is measured in keV, the slope $\alpha_{\rm TM} = 0.65 \pm 0.03$ and $\beta_{\rm TM} = (3.02 \pm 0.11) \times 10^{14}\, h^{-1}\, {\rm M}_\odot$. The symbol $\sigma_{\rm TM}$ is the scatter in $\ln T_{\rm X}$ at fixed mass, and reads $\sigma_{\rm LM} \simeq 0.119$ (see Table 1). This value is derived from numerical simulations (Kravtsov et al. 2006) and we assume a lognormal distribution also for the conditional probability of getting $T_{\rm X}$ given M_{500}, in analogy with equation (19). The fit in equation (20) holds for relaxed clusters only: to take into account unrelaxed morphologies, the estimated mass from equation (20) should be multiplied by a factor of 1.17. We do not implement this correction. For the metal abundance, we choose a value of 0.3 relative to solar abundance (Anders & Grevesse 1989), which is typical for nearby clusters, with little or no evolution to higher redshifts (Tozzi et al. 2003). We use the *apec* model (Smith et al. 2001) within XSPEC (Arnaud 1996, version 12.5.1n) to model the emitted spectrum (thermal bremsstrahlung, recombination emission, as well as bound–bound transitions from collisionally ionized, optically thin plasma), for given temperature, metal abundance, luminosity and redshift.

(ii) The photoelectric absorption can be modelled using the hydrogen column density along the line of sight, $N_{\rm H}$, and assuming the associated abundance of helium and heavy elements. For this, we use the *phabs* model within XSPEC (with the default cross-sections), in order to self-consistently use the same metal abundances as above. The Galactic $N_{\rm H}$ varies across the sky. We use recent data from 21-cm radio measurements provided by Peter Kalberla (the Leiden–Argentine–Bonn, LAB, survey; Kalberla et al. 2005) and determine the $N_{\rm H}$ distribution, excising $\pm 20^\circ$ around the Galactic plane. We find that 3×10^{20} atoms cm^{-2} is a typical value, which we adopt throughout.

(iii) We model the *eROSITA* response using the latest preliminary matrices provided by Frank Haberl.[10] In particular, we use the file erosita_iv_7telfov_ff.rsp, which takes into account the CCD quantum efficiency and filter transmission, as well as the mirror area of all seven telescopes, averaged over the field of view. The response of *eROSITA* in terms of count rates is shown in Fig. 1 for some characteristic redshifts and for a cluster luminosity of $L_{\rm X} = 10^{45}$ erg s^{-1}.

(iv) The exact orbit and scanning strategy of *eROSITA* are currently under investigation. We consider two different versions of the expected 4-yr all-sky exposure map kindly provided by Jan Robrade. We exclude $\pm 20^\circ$ around the Galactic plane.

We then calculate the average exposure in the remaining area, which results in 2.4 ks, for both exposure map versions. This exposure assumes 100 per cent efficiency. For a more realistic estimate, we need to multiply 2.4 ks by a factor smaller than 1. This factor is rather uncertain at this time. An optimistic value is 0.8, a pessimistic one $0.8 \times 0.67 = 0.54$ (the factor 0.67 is supposed to account for soft proton flares, which are expected at *eROSITA*'s L2 orbit). Therefore, we expect $1.3 < T_{\rm exp} < 1.9$ ks. We assume 1.6 ks as a realistic estimate of the average exposure time, unless specifically mentioned otherwise.

Once $L_{\rm X}$, $T_{\rm X}$ and z are known, we are thus able to compute the expected photon counts $\bar{\eta}_{\rm fid}(L_{\rm X}, T_{\rm X}, z)$ within XSPEC for our fiducial reference cosmology. Since η depends on the assumed cosmology

[10] http://www.mpe.mpg.de/erosita/response/

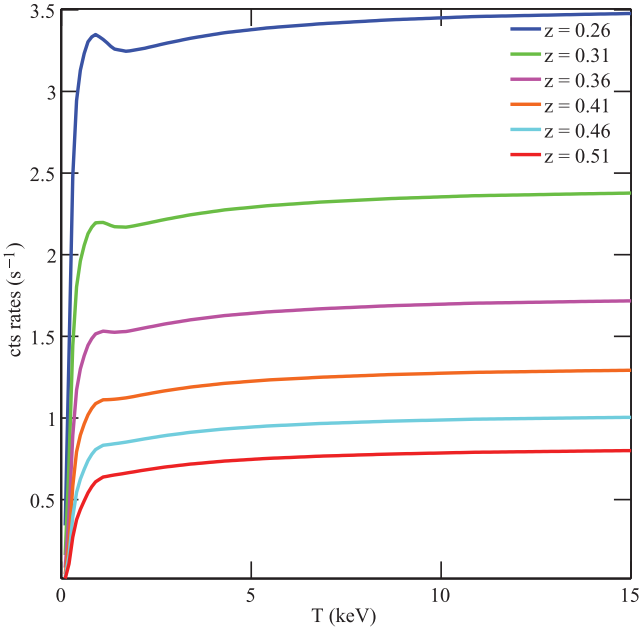

Figure 1. Characteristics of the *eROSITA* telescope: *eROSITA* response (rate of X-ray photons counted in the detector) in the (0.5–2.0) keV energy band (observer frame), for a source of luminosity $L_{\rm X} = 10^{45}$ erg s^{-1} in the (0.5–2.0) keV rest-frame band, at different redshifts, $z = 0.26, 0.31, \ldots$, from top to bottom.

through the luminosity distance $D_{\rm L}$, we scale the photon counts according to $\bar{\eta} = \bar{\eta}_{\rm fid} D^2_{\rm L,fid}/D^2_{\rm L}$, every time the assumed cosmology is varied. We also account for the statistical uncertainty in the photon counts by assuming that they follow Poisson statistics. In brief, the probability distribution of the counts is

$$P(\eta|M,z) = \int {\rm d}L_{\rm X}\, {\rm d}T_{\rm X}\; P[\eta|\bar{\eta}(L_{\rm X}, T_{\rm X}, z)]\; P(L_{\rm X}, T_{\rm X}|M, z)\;, \quad (21)$$

where η is a Poisson variate of mean $\bar{\eta}$ and P generically denotes any probability density function. It is interesting to consider the possibility that there is a correlation between the X-ray temperature and luminosity for clusters of a given mass. In fact, this would reduce the scatter in the distribution of η at fixed mass. We write the joint conditional probability $P(L_{\rm X}, T_{\rm X}|M, z)$ as a bivariate lognormal distribution:

$$P(\boldsymbol{X}|M) = \frac{1}{2\pi|\boldsymbol{\Sigma}|^{1/2}} \exp\left[-\frac{1}{2}(\boldsymbol{X}-\boldsymbol{\mu})^{\rm T}\boldsymbol{\Sigma}^{-1}(\boldsymbol{X}-\boldsymbol{\mu})\right], \quad (22)$$

where the vector $\boldsymbol{X}$ and its covariance matrix read

$$\boldsymbol{X} = \begin{pmatrix} \ln L_{\rm X} \\ \ln T_{\rm X} \end{pmatrix} \text{ and } \boldsymbol{\Sigma} = \begin{pmatrix} \sigma^2_{\rm LM} & \rho_{\rm LT}\sigma_{\rm LM}\sigma_{\rm TM} \\ \rho_{\rm LT}\sigma_{\rm LM}\sigma_{\rm TM} & \sigma^2_{\rm TM} \end{pmatrix}. \quad (23)$$

Here $\boldsymbol{\mu}$ refers to the mean values of the scaling relations and $\rho_{\rm LT}$ is the linear correlation coefficient between the residuals in luminosity and temperature. Theoretically, it is expected that $L_{\rm X}$ and $T_{\rm X}$ may be highly correlated (Stanek et al. 2010) or anticorrelated (Kravtsov et al. 2006); on the other hand, data for a set of clusters drawn from the *ROSAT* all-sky survey with *Chandra* follow-up show no evidence of a correlation (Mantz et al. 2010a). If we assume that $L_{\rm X}$ and $T_{\rm X}$ are independent variables and naively combine the mass–luminosity and mass–temperature relations from Vikhlinin et al. (2009a), we find that the (intrinsic) scatter in luminosity at fixed $T_{\rm X}$ should be $\sim$0.49 (in the ln–ln plane). In case of a positive correlation among the variables, this scatter should be smaller. Direct measurements of the scatter from the Representative XMM–Newton

Cluster Structure Survey (REXCESS) (Pratt et al. 2009) give 0.276 for core-excised clusters and 0.666 when the cluster cores are included. On the other hand, other studies of the 64 brightest clusters in the sky Highest X-Ray Flux Galaxy Cluster Sample (HIFLUGCS), see Mittal et al. 2011) suggest a reduced importance of cool cores as scatter contributors and an intrinsic scatter in the L_X–T_X relation of 0.455 for the whole sample. Estimating the degree of correlation by directly comparing these figures is thus inconclusive and better data are needed. We have initially attempted to include ρ_{LT} in the set of parameters that we would like to constrain with *eROSITA*. However, we found out that the weak dependence of the photon counts, η, on T_X (see Fig. 1) makes all the observables rather insensitive to ρ_{LT} which remains unconstrained by the data. To simplify the analysis, we thus assume $\rho_{LT} \equiv 0$.

The resulting photon counts as a function of cluster mass and redshift are shown in the upper-left panel of Fig. 2. This gives

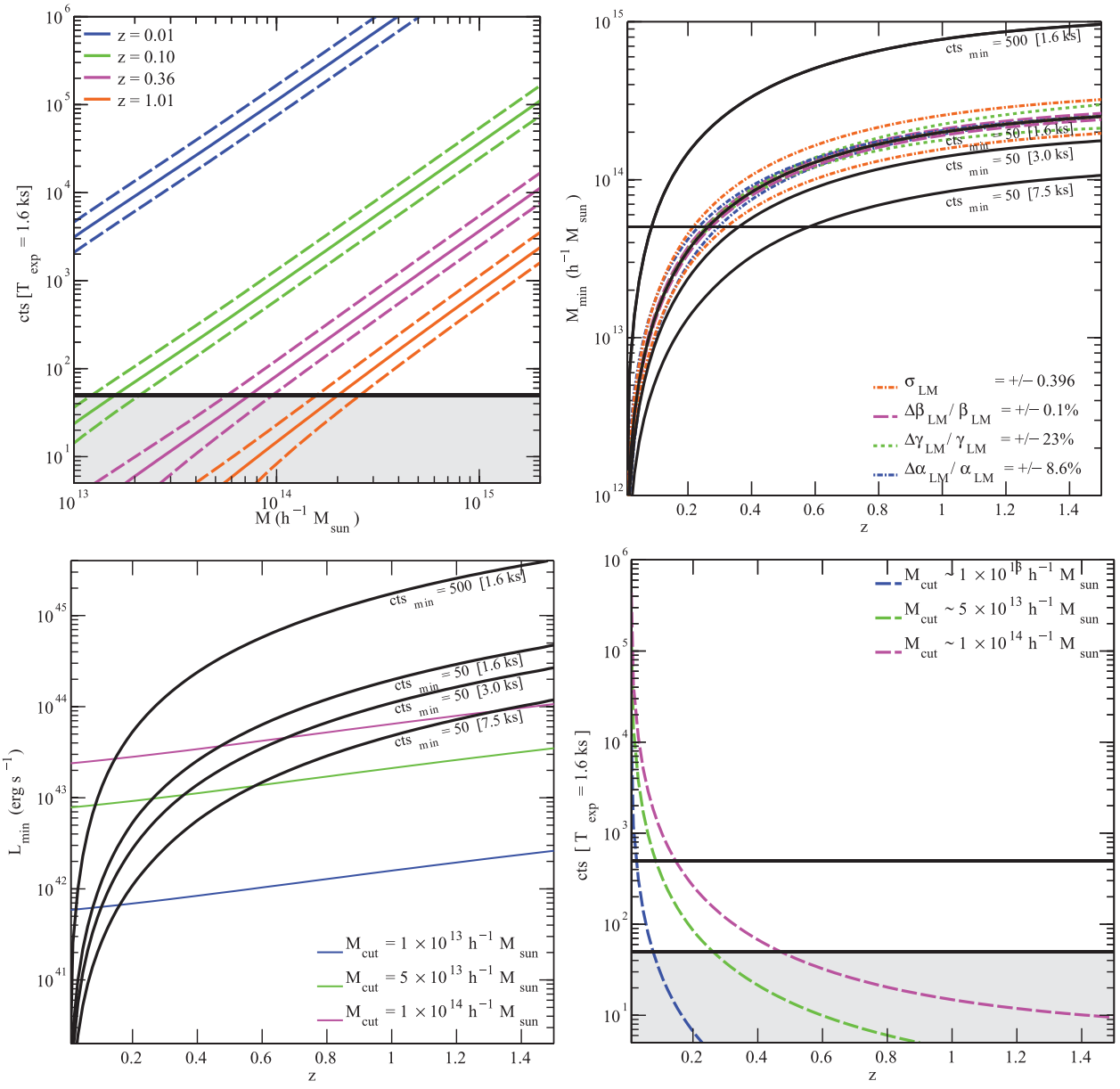

Figure 2. Observable–mass relation and sample selections for the *eROSITA* galaxy clusters. Top-left panel: effective photon count versus mass relation (η–M_{500}) derived via equation (21). The solid curves indicate the mean relation at $z \simeq 0.01, 0.10, 0.36$ and 1.51, from top to bottom, along with a 68 per cent level of scatter encompassed by the dashed lines (corresponding to about ± 41 per cent symmetrized relative error in the range of interest). The black solid line marks the detection threshold of 50 photons. Top-right panel: mass threshold (M_{500}) corresponding to different photon-count detection limits as a function of redshift. We choose 50 photons with an integration time of 1.6 ks as our reference choice. The thick horizontal line indicates the additional cut at $M = 5 \times 10^{13}\, h^{-1}\, M_\odot$ which we impose to avoid considering clusters that possibly do not obey power-law scaling relations or exhibit a mass-dependent scatter. The coloured curves show the effect that the current uncertainties on the parameters of the LM relation (see legend) would have on the determination of the detection limit. Bottom-left panel: threshold luminosity as a function of redshift, for different photon-count detection limits. The coloured lines indicates the position of the additional possible mass cuts in the luminosity–redshift plane (see legend). Bottom-right panel: selection criteria in the η–z plane. The black solid lines correspond to the detection thresholds of 50 and 500 photons; the coloured curves connect points corresponding to a given mass limit (colours as in the left-hand panel).

an effective η–M_{500} relation which scales as M^{α} with $\alpha \sim 1.60$–1.65 (depending on redshift). The scatter in our observable–mass relation at fixed mass is dominated by $\sigma_{\rm LM}$, but also depends on $\sigma_{\rm TM}$ and the Poisson noise in the photon counts. This corresponds to a (symmetrized) relative uncertainty at fixed mass of about 41 per cent at $z \sim 0.1$; at $z \sim 1$ this ranges between 66 and 41 per cent for objects with $M \gtrsim 5 \times 10^{13}\, h^{-1}\, {\rm M}_{\odot}$.

5 THE *eROSITA* EXPERIMENT

For our purposes, we characterize the *eROSITA* survey using three numbers: the fraction of the sky covered by the experiment $f_{\rm sky}$, the exposure time $T_{\rm exp}$, and the detection threshold in raw photon counts $\eta_{\rm min}$ (see Table 1). We take as a reference an all-sky survey covering more than 27 000 deg^2 and with an average exposure time of $\sim$1.6 ks; moreover, we limit our analysis to the (0.5–2.0) keV X-ray energy band, such that all the figures in this work have to be considered in that band. This all-sky survey should exquisitely constrain model parameters, since it will simultaneously provide robust statistics ($\sim 10^5$ galaxy clusters detected with more than 50 photons) and sample very large spatial scales where primordial non-Gaussianity is expected to leave its strongest imprints ($k \lesssim 0.01 h\, {\rm Mpc}^{-1}$). As a reasonable source-detection threshold, we choose $\eta = 50$ counts as the default. This number is motivated by the experience from the *ROSAT* All-Sky Survey (RASS), where the count limit has typically been set at (10–30) photons in scientific analyses of cluster catalogues, e.g. Schuecker et al. (2001). In the future, this limit will be tested against detailed simulations of the *eROSITA* survey. While 50 source counts are sufficient for a luminosity determination, one could measure the intracluster gas mass already with about 500 source counts. The gas mass is a better proxy of the total gravitational mass than the luminosity, so when applying the 500 count limit one could in practice assume a smaller scatter in the observable–mass relation. While in this section we discuss both cluster samples determined using these different thresholds, the whole statistical analysis of Sections 7 and 8 will be performed with the cut of 50 photons.

Low-redshift objects which are fainter than 10^{42} erg s^{-1} could in principle be detected with more than 50 photon counts with an average exposure time of 1.6 ks (Fig. 2, bottom-left panel). This corresponds to masses smaller than $\sim 10^{13}\, h^{-1}\, {\rm M}_{\odot}$ at $z \lesssim 0.1$ (Fig. 2, upper-left and upper-right panels). Although scaling-relation studies which extend towards masses of $\sim 10^{13}\, h^{-1}\, {\rm M}_{\odot}$ are available (Sun et al. 2009; Eckmiller, Hudson & Reiprich 2011), the adopted prescriptions from Vikhlinin et al. (2009a) are obtained from a cluster sample limited at about $7 \times 10^{13}\, h^{-1}\, {\rm M}_{\odot}$. Moreover, the scatter in the observed relations increases for low-mass clusters and groups (Eckmiller et al. 2011): this would necessitate to introduce a mass-dependent scatter in our analysis. For these reasons, in addition to the photon cut of 50 photons assumed for cluster detection, we add a redshift-dependent luminosity cut, which is effective in the low-redshift part ($z \lesssim 0.25$) to remove low-mass systems ($M < 5 \times 10^{13}\, h^{-1}\, {\rm M}_{\odot}$); see Fig. 2, upper-right and bottom-left panels. In practice, we pick our fiducial cosmology and our fiducial luminosity–mass relation as a function of z and we look for a redshift-dependent luminosity cut that corresponds to the desired minimum mass; this, in turn, results into a redshift-dependent η cut (Fig. 2, bottom-right panel) which is model-independent and which can be easily applied to real data (while a true-mass cut cannot), if redshift information is available.[11] Note that neither a luminosity cut nor a mass cut are in practice applied here; low-mass objects are removed solely referring to the unique curve in the η–z plane which corresponds to the chosen mass threshold in the fiducial model (Fig. 2, bottom-right panel); such cut is kept fixed throughout the statistical analysis independently of the assumed values for the cosmology and scaling-relation parameters (see Section 9.5).

In Fig. 2, we compare a series of photon-count thresholds ($\eta = 50$ and 500 photons with $T_{\rm exp} = 1.6$ ks, and $\eta = 50$ photons with $T_{\rm exp} = 1.6$, 3.0, 7.5 ks) and additional luminosity cuts (corresponding to masses of $\sim 1, 5, 10 \times 10^{13}\, h^{-1}\, {\rm M}_{\odot}$), in the M_{500}–z plane (upper-right panel), in the $L_{\rm X}$–z plane (bottom-left panel) and in the η–z plane (bottom-right panel). Fig. 2 shows that, away from the Galactic plane, *eROSITA* will detect *all* clusters more luminous than $\sim 5 \times 10^{44}$ erg s^{-1} up to $z \sim 1.5$, namely all massive ($M \gtrsim 3 \times 10^{14}\, h^{-1}\, {\rm M}_{\odot}$) clusters in the observable Universe.

In the left-hand panel of Fig. 3, we show the redshift distribution of the population of clusters detected by *eROSITA* [see Section 5 and equation (24), for details]: the solid black curve is the redshift distribution of all the galaxy clusters above the cut of 50 photons for $T_{\rm exp} = 1.6$ ks; the corresponding total number of objects in the whole sky ($f_{\rm sky} \equiv 0.658$) is $\sim 1.37 \times 10^5$ objects. In the same panel, the dashed curves indicate the redshift distributions of the same population of clusters once the additional cuts are applied. The integrated number of objects reduces to $\sim 9.32 \times 10^4$ and the median redshift shifts to $\sim$0.35 when objects below $5 \times 10^{13}\, h^{-1}\, {\rm M}_{\odot}$ are removed. We summarize our findings in Table 2. To facilitate comparisons with other works using different observables from raw photon counts, we show in the right-hand panel of Fig. 3 the cumulative mass distribution of clusters above our detection threshold of 50 counts, as function of z and M_{500}.

Finally, in Fig. 4, we compare the selections discussed so far with an alternative flux-based selection, often employed in X-ray cluster surveys. Two cases are shown: a comparison with a 50-photon limit (main box) and with a 500-photon limit (smaller inbox). The solid curves show the fraction of objects which pass a threshold both in flux and in photon counts with respect to the objects which pass a threshold set only in terms of flux. Minimum fluxes of 3.2, 4.2, 4.4 $\times 10^{-14}$ erg s^{-1} cm^{-2} in the (0.5–2.0) keV energy band would result, respectively, in 68, 90, 95 per cent completeness levels for $\eta_{\rm min} = 50$. For $\eta_{\rm min} = 500$, 68, 90, 95 per cent completeness is reached with flux limits of 3.5, 4.4, 4.6 $\times 10^{-13}$ erg s^{-1} cm^{-2}, respectively.

6 OBSERVABLES

The measurements that we consider are galaxy-cluster abundances and angular clustering. In this section we study their sensitivity to the actual values assumed by the model parameters.

Fig. 5 shows how the *eROSITA* number counts depend on the cosmological parameters and on the parameters characterizing the physics of the ICM. In the upper panels of Fig. 5, the 'count function' dn/dη at the median redshift of the sample is shown for our fiducial model (black solid line) and for alternative models where

[11] In order to apply this additional cut, redshift measurements are only required for $z \lesssim 0.25$ where, most likely, no new clusters will be discovered by *eROSITA*. Therefore, this sample selection should be easily feasible in practice.

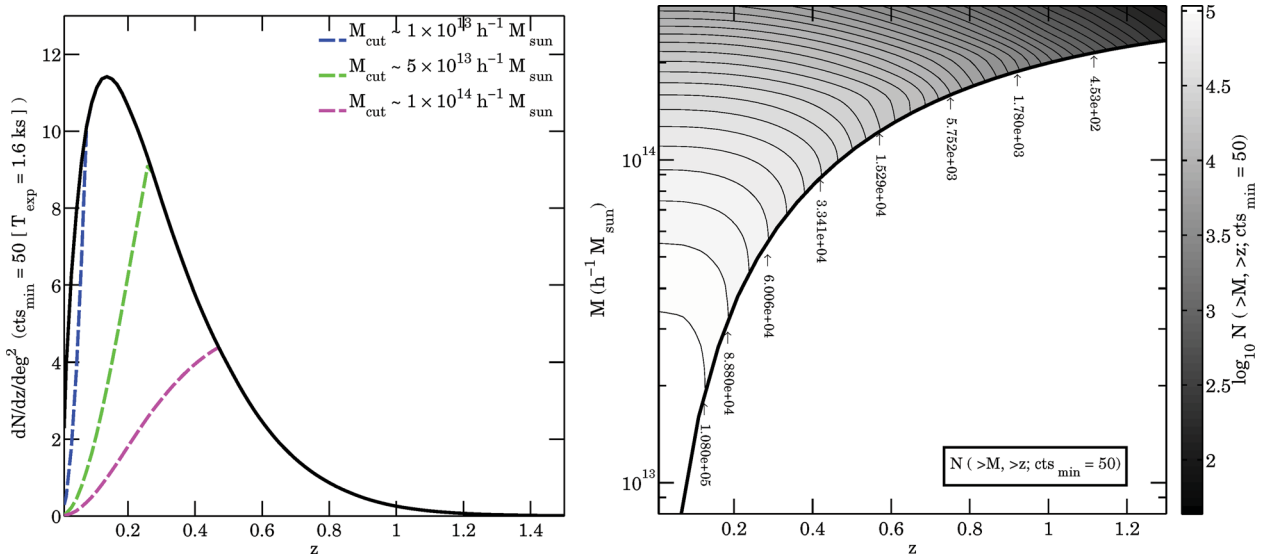

Figure 3. Left: redshift distribution of *eROSITA* clusters for different minimum masses (colour-coded as in the bottom panels of Fig. 2). Right: number of clusters passing the detection threshold of 50 counts, as a function of redshift and M_{500}, with sky coverage fraction $f_{\rm sky} = 0.658$.

Table 2. Number of galaxy clusters detected by *eROSITA* and their median redshift for the all-sky survey, with sky coverage fraction $f_{\rm sky} = 0.658$.

	$N_{\rm clusters}$ ($\eta_{\rm min} = 50$, $T_{\rm exp} = 1.6$ ks)	$z_{\rm median}$
All objects	1.37×10^5	0.25
$M \gtrsim 1 \times 10^{13}$ ($h^{-1}\,{\rm M}_\odot$)	1.31×10^5	0.27
$M \gtrsim 5 \times 10^{13}$ ($h^{-1}\,{\rm M}_\odot$)	9.32×10^4	0.35
$M \gtrsim 1 \times 10^{14}$ ($h^{-1}\,{\rm M}_\odot$)	5.57×10^4	0.46

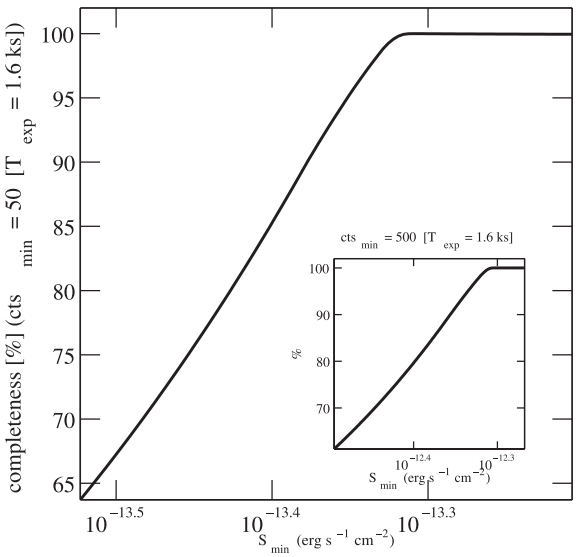

Figure 4. Completeness of a survey limited in flux and photon counts with respect to a purely flux-limited selection with $S > S_{\rm min}$ for a 50-photon limit (main panel) and 500-photon limit (inset).

the cosmological (left) and ICM (right) parameters are varied (one at the time) by the current uncertainty (listed in Table 1).

The redshift distribution of the clusters above the detection threshold of $\eta_{\rm min} = 50$ counts with $T_{\rm exp} = 1.6$ ks relates to the count function as follows:

$$\frac{{\rm d}N}{{\rm d}z\,{\rm deg}^2}(>\eta_{\rm min}, z) = \frac{4\pi}{A} f_{\rm sky} \left[\frac{c}{H(z)} D_{\rm A}^2(z)\right] \int_{\eta_{\rm min}}^{\infty} \frac{{\rm d}n}{{\rm d}\eta}(\eta, z)\,{\rm d}\eta, \quad (24)$$

where A is the survey area in deg^2, c is the speed of light and $D_{\rm A}$ is the comoving angular diameter distance (which coincides with r for flat universes). The total number of clusters detected above a certain detection threshold can be calculated by integrating the equation above over redshift and multiplying the result by A.

The bottom panels of Fig. 5 give the relative change of the observables with respect to the fiducial model. The largest deviations are due to changes in σ_8, $\Omega_{\rm m}$ and $f_{\rm NL}^{\rm local}$, and all the four parameters of the LM relation. All parameters but $n_{\rm s}$ and h generate larger uncertainties at higher redshifts than at lower redshifts (not shown). Note that changing σ_8 within the current uncertainty modifies the cluster counts by 20 per cent for objects detected with more than $\sim$400 photons at the median redshift, or for all the objects above $z \gtrsim 0.6$. Also primordial non-Gaussianity (with positive $f_{\rm NL}^{\rm local}$) has a stronger impact at higher redshifts and for higher photon counts. The effects of the Hubble constant and of the scalar spectral index exceed the per cent level only for the brightest clusters, e.g. above a few 10^3 photon counts around the median redshift, which already suggests that binning the *eROSITA* data in η should better constrain these parameters. Current uncertainties in the parameters regulating the temperature–mass relation (not shown but discussed in Section 11.3) affect the cluster counts at the per cent or sub-per cent level thus indicating that *eROSITA* counts will hardly be able to put interesting constraints on those parameters. Finally, we have checked that fitting errors in the parameters of the Tinker mass function (not shown but discussed in Section 11.1) also give sub-per cent modifications. This confirms that our theoretical framework is robust.

We now consider the spatial clustering of the detected clusters. Imagine to split the *eROSITA* sample into bins (based on the cluster redshift or photon counts). The angular cross-spectrum between the

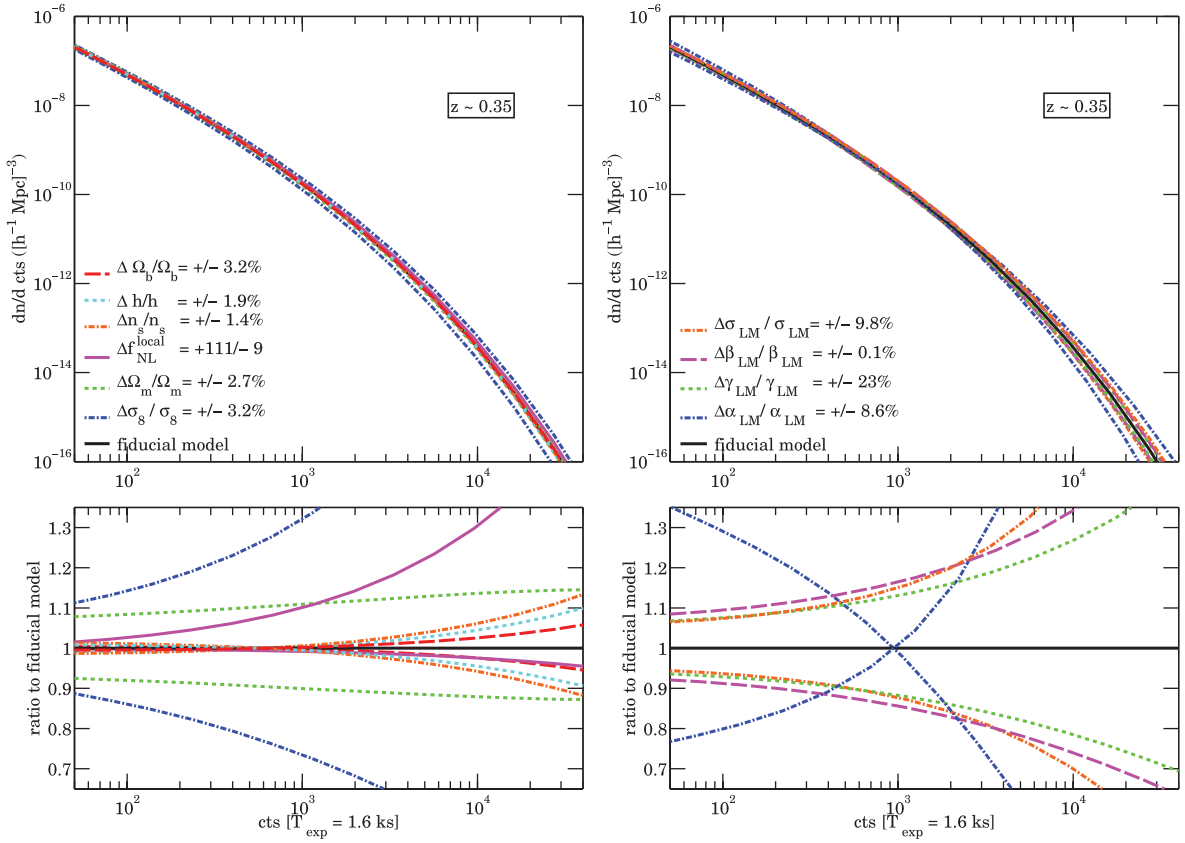

Figure 5. Number counts of *eROSITA* clusters. The black solid line refers to our fiducial model while the other lines show the dependence on the cosmological parameters (left) and on the parameters of the LM scaling relation (right), varied one at the time of the relative amounts indicated in the legend (variations correspond to the current uncertainties on the parameters as indicated in Table 1).

pair of bins i, j can be written as

$$C_\ell(i,j) = \frac{2}{\pi}\int_0^\infty \mathrm{d}k\, k^2 \int_0^\infty \mathrm{d}r_1\, W_i(r_1,k)\, j_\ell(kr_1) \times \int_0^\infty \mathrm{d}r_2\, W_j(r_2,k)\, j_\ell(kr_2)\, P_{\rm NL}(k,r_1,r_2), \quad (25)$$

where the functions $W_i(r,k)$ are defined as

$$W_i(r,k) = \frac{1}{N_i}\frac{\mathrm{d}N_i}{\mathrm{d}r}(r)\, b_i[k,z(r)], \quad (26)$$

and N_i is the total number of objects within the ith bin, j_ℓ denotes the spherical Bessel function of the first type and $b_i[k, z(r)]$ is the effective bias of the cluster population (obtained by averaging equation (13) over halo mass or photon counts and weighting by the number density) in the ith bin. Here $P_{\rm NL}$ denotes the cross-spectrum between the matter distribution at two different redshifts, z_1 and z_2, corresponding to the comoving distances, $r_1(z_1)$ and $r_2(z_2)$.

In Fig. 6 the dependence of the angular power spectrum on the cosmological and ICM parameters is shown for galaxy clusters with $\eta \geq 50$ and lying within the broad redshift range [0.1–1.5]. Note that the largest modifications in the signal are driven by the current uncertainties in σ_8, $\Omega_{\rm m}$, $f_{\rm NL}^{\rm local}$ and $\gamma_{\rm LM}$. An accurate determination of the cluster power spectrum with *eROSITA* has therefore the potential to strongly constrain these model parameters.

To speed up calculations, it is convenient to rewrite equation (25) using the Limber approximation:

$$C_\ell(i,j) \simeq 4\pi \int_0^\infty \mathrm{d}z\, \frac{\mathrm{d}V}{\mathrm{d}z}\, P_{\rm NL}\left(\frac{\ell+1/2}{D_{\rm A}}, z\right)\, W^i_{\ell,{\rm L}}(z)\, W^j_{\ell,{\rm L}}(z), \quad (27)$$

with the Limber weight functions $W^i_{\ell,{\rm L}}$ being defined as

$$W^i_{\ell,{\rm L}}(z) = \frac{1}{N_i}\frac{\mathrm{d}N_i}{\mathrm{d}V}(z)\, b_i\left(\frac{\ell+1/2}{D_{\rm A}}, z\right), \quad (28)$$

where V is the comoving volume. We use equation (25) for all multipoles with $\ell \lesssim 100$ and equation (27) for larger values of ℓ. A motivation for this choice and a critical discussion about the limitations of the Limber approximation in the presence of primordial non-Gaussianity will be given in Section 11.4.

6.0.1 *The choice of ℓ_{min}*

Primordial non-Gaussianity of the local type modifies the shape of the angular power spectrum of galaxy clusters by introducing a scale-dependent bias on very large scales (see Fig. 6). Therefore, experimental constraints on $f_{\rm NL}^{\rm local}$ improve by measuring clustering at larger and larger scales. However, the correlation function of biased tracers of the cosmic density field in scenarios with $f_{\rm NL}^{\rm local} \neq 0$ formally diverges for every spatial separation if Fourier modes down to $k \to 0$ are considered (e.g. Wands & Slosar 2009). This is because the biased density field has infinite variance [as like as the gravitational potential which generates the scale-dependent bias (see Giannantonio & Porciani 2010)]. Any observed correlation function, anyway, will be finite because density fluctuations on scales larger than the survey are not observable. Fluctuations are always defined with respect to the mean density as measured from the same survey, thus forcing their average to zero. The expectation value of the observed correlation therefore departs from the underlying one

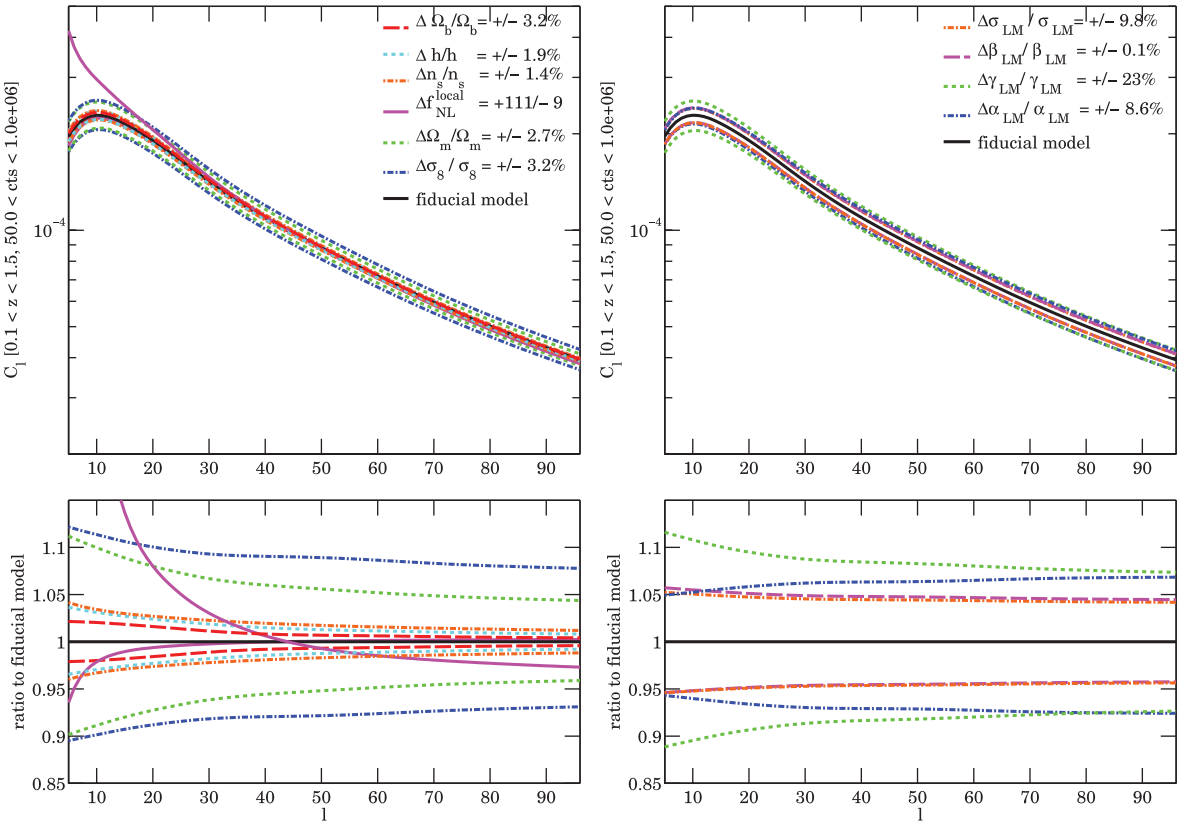

Figure 6. Angular power spectrum of *eROSITA* clusters and its dependence on the cosmological and ICM parameters. The signal refers to clusters detected with $\eta \geq 50$ photons ($T_{\rm exp}$ =1.6ks) within the redshift range $0.1 < z < 1.5$.

by a constant shift (sometimes known as the 'integral constraint') which is finite only if $f_{\rm NL}^{\rm local} = 0$. In practice, this effect is taken into account by including the window function of the survey in the calculation of C_ℓ. This regularizes all the integrals. For simplicity, here we approximate the influence of the window function by using a high-pass filter $k > k_{\rm min} \sim 10^{-3} h\,{\rm Mpc}^{-1}$ and only considering a minimum order for the spherical harmonics $\ell_{\rm min}$ so that the derivatives in the Fisher matrix do not depend on $k_{\rm min}$ (see also Cunha et al. 2010). In what follows, we will use $\ell_{\rm min} = 5$ for the *eROSITA* all-sky survey, and $\ell_{\rm min} = 7$–10 for the deeper surveys presented in Section 9.1. These choices are motivated as follows. First, multipoles with $\ell < 10$ cannot be precisely measured if $f_{\rm sky}$ substantially departs from unity, since only a few modes are available in the whole sky. Secondly, evaluating C_ℓ at such low multipoles requires knowledge of the halo bias at wavenumbers $k \ll 0.01 h\,{\rm Mpc}^{-1}$, never probed by N-body simulations. Pushing the analysis to $\ell \sim 3$ would imply trusting the extrapolation of the non-Gaussian halo bias of equation (13) down to $k \sim 10^{-4} h\,{\rm Mpc}^{-1}$ where also general-relativity corrections certainly become very important (e.g. Yoo 2010; Baldauf et al. 2011).

6.0.2 *The choice of ℓ_{max}*

We also have to set a minimum angular scale that will be considered in the clustering analysis. This is mainly dictated by the limitations of the theoretical models for the angular power spectrum of galaxy clusters. Angular multipoles and wavenumbers are related through the angular diameter distance in a redshift-dependent fashion. The choice of the maximum multipole thus corresponds to selecting the largest wavenumber that we want to consider, $k_{\rm max}$. Three issues have to be taken into account: cluster exclusion effects, dynamical non-linearity of density perturbations and non-linearity of the DM halo bias. We compare the characteristic scales of these three effects in Fig. 7. Galaxy clusters are extended objects (at $z \sim 0.35$, a spherical $10^{14}\,h^{-1}\,{\rm M}_\odot$ cluster has a comoving R_{500} of about 0.6 h^{-1} Mpc) and their spatial separation cannot be much smaller than their characteristic size ($\sim 2R_{500}$). This imprints a sharp drop in the amplitude of C_ℓ at small angular scales which is difficult to model accurately. The blue dashed curve in Fig. 7 indicates the characteristic size (and thus, roughly, the minimum separation) of objects with $M \sim 10^{14}\,h^{-1}\,{\rm M}_\odot$. Regarding the non-linearity of the matter-density field, we do not want to rely on approximate prescriptions for the matter power spectrum on mildly non-linear scales which could compromise the accuracy of the fits for the cosmological parameters. The onset of the non-linear regime for the matter power spectrum can be approximately evaluated by determining $k_{\rm max}(z)$, such that

$$\sigma^2(k_{\rm max}, z) = \frac{1}{2\pi^2} \int_0^{k_{\rm max}(z)} k^2\, P_{\rm lin}(k, z)\, {\rm d}k = 0.5. \qquad (29)$$

The solid black line in Fig. 7 shows the function $k_{\rm max}(z)$. Similarly, we are concerned with the linearity of cluster bias. Equations (12) and (13) asymptote to a constant value for $k \to \infty$. However, N-body simulations show that on sufficiently small scales (depending on redshift and mass), the bias of DM haloes departs from a constant thus becoming non-linear. For haloes with mass $M \gtrsim 5 \times 10^{13}\,h^{-1}\,{\rm M}_\odot$ at $z \sim 0$, the non-linear regime of the bias kicks in for wavenumbers above $k \sim 0.1$–$0.3\,h\,{\rm Mpc}^{-1}$. This threshold

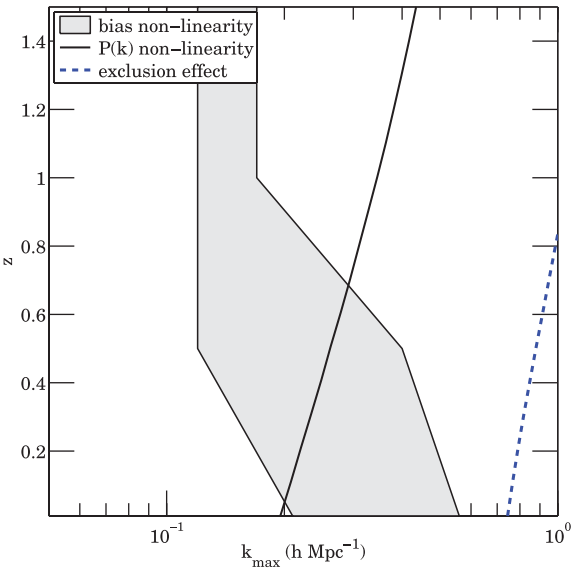

Figure 7. Maximum wavenumber which can be robustly modelled in the power-spectrum study, as a function of redshift. The blue dashed line refers to exclusion effects and indicates the minimum separation allowed for (spherical) objects of $\sim 10^{14}\,h^{-1}\,\mathrm{M}_\odot$. The black solid line marks the onset of the non-linear regime for density perturbations (see main text for details). The grey area approximately traces the minimum wavenumber (as a function of redshift) at which a scale-dependence in the bias of DM haloes of mass $\sim 3\times 10^{13} \lesssim M \lesssim 2\times 10^{14}\,h^{-1}\,\mathrm{M}_\odot$ can be detected in the numerical simulations of Pillepich, Porciani & Hahn (2010). Note that, for galaxy clusters, the most severe requirement comes from the non-linearity of the bias. To overcome this problem, in our study we only consider wavenumbers such that $k < k_{\rm max} = 0.1\,h\,\mathrm{Mpc}^{-1}$.

decreases with redshift and mass. The grey band in Fig. 7 indicates an approximate determination of the onset of non-linearities in the bias for DM haloes in the mass range (3–20) $\times\ 10^{13}\,h^{-1}\,\mathrm{M}_\odot$, as extracted from the *N*-body simulations of Pillepich et al. (2010). The numerical work by Manera et al. (2010) shows that for objects with $M \gtrsim 10^{14}\,h^{-1}\,\mathrm{M}_\odot$ the transition occurs at even slightly smaller wavenumbers. In summary, at all redshifts greater than 0.1, the linearity of the bias gives the most stringent constraints, followed by the linearity of the density field. Based on these arguments, we make a conservative choice and adopt a maximum wavenumber of $k_{\rm max} = 0.1\,h\,\mathrm{Mpc}^{-1}$, which corresponds to $\ell_{\rm max} \sim 96$ at the median redshift of the all-sky survey. We relax this choice in Section 11.5.

7 FISHER-INFORMATION FORMALISM

The Fisher-matrix formalism (Tegmark, Taylor & Heavens 1997) is a tool for forecasting how well a future experiment will constrain some model parameters. Given a data set, $\boldsymbol{x}$, and a set of parameters $\boldsymbol{\theta}$ with fiducial values, $\boldsymbol{\theta}_0$, we define the Fisher information matrix as

$$F_{\alpha\beta} = \left\langle \frac{\partial^2 \mathcal{L}}{\partial\theta_\alpha \partial\theta_\beta} \right\rangle, \tag{30}$$

where the average is taken over an ensemble of realizations of the experiment and $\mathcal{L} = -\ln L$ with $L(\boldsymbol{x};\boldsymbol{\theta})$ being the likelihood of the data given a model. For unbiased estimators, $\langle\hat{\boldsymbol{\theta}}\rangle = \boldsymbol{\theta}_0$ (where $\hat{\boldsymbol{\theta}}$ denotes an estimate of the parameter set based on a single realization of the experiment), the inverse of the Fisher matrix (evaluated at $\boldsymbol{\theta} = \boldsymbol{\theta}_0$) provides an approximation for the covariance matrix of the model parameters:

$$\Sigma^{\rm param}_{\alpha\beta} = (F^{-1})_{\alpha\beta}. \tag{31}$$

Under some weak regularity conditions, the Cramér–Rao inequality assures that the marginal errors of the model parameters follow

$$\sigma_\alpha \geq (F^{-1})^{1/2}_{\alpha\alpha}, \tag{32}$$

while the conditional errors (i.e. the errors that would be obtained keeping all the other parameters fixed) will be larger or equal than $1/\sqrt{F_{\alpha\alpha}}$.

For a (multivariate) Gaussian likelihood function $L(\boldsymbol{x};\boldsymbol{\theta})$, the Fisher matrix can be explicitly written as

$$F_{\alpha\beta} = \frac{1}{2}\mathrm{Tr}\left[\boldsymbol{\Sigma}^{-1}(\boldsymbol{\mu}_{,\alpha}\,\boldsymbol{\mu}^{\rm T}_{,\beta} + \boldsymbol{\mu}_{,\beta}\,\boldsymbol{\mu}^{\rm T}_{,\alpha}) + \boldsymbol{\Sigma}^{-1}\boldsymbol{\Sigma}_{,\alpha}\,\boldsymbol{\Sigma}^{-1}\boldsymbol{\Sigma}_{,\beta}\right], \tag{33}$$

where $\boldsymbol{\mu} = \langle\boldsymbol{x}\rangle$, $\boldsymbol{\Sigma} = \langle(\boldsymbol{x}-\boldsymbol{\mu})(\boldsymbol{x}-\boldsymbol{\mu})^{\rm T}\rangle$, and commas denote partial derivatives with respect to the model parameters. If $\mathcal{M}$ is the number of model parameters and $\mathcal{N}$ is the number of data points, the Fisher matrix is a $\mathcal{M}\times\mathcal{M}$ matrix while $\boldsymbol{\Sigma}$ is $\mathcal{N}\times\mathcal{N}$. The trace operator in equation (33) acts on the $\mathcal{N}$-dimensional space of data points.

If different experiments are independent, the total Fisher matrix is the sum of individual Fisher matrices. 'Adding priors' can be regarded here as adding the Fisher matrix of a third experiment.

7.1 Figure of merit

In order to compare individual probes, optimize the experiments and quantify their individual performance in constraining model parameters, we introduce the (total) figure of merit (FoM), defined as

$$\mathrm{FoM} = \log_{10}\left[\det(\mathrm{F}^{-1})\right]^{-1/2}. \tag{34}$$

This is inversely proportional to the volume of the $\mathcal{M}$-dimensional error hyper-ellipsoid. The higher the FoM, the more suitable an experiment is to constrain our selected parameter set. For example, halving uniformly all the parameter errors would correspond to an increment in the FoM of $\log_{10}\left(2^{\mathcal{M}}\right)$, which for $\mathcal{M} = 10$ reads ~ 3. Similarly, if one wants to focus on a selected subset of parameters, a (partial) FoM can be defined by considering a Fisher matrix of lower dimensionality.

7.2 Number counts

For an unclustered point process, the probability of counting N_i objects in the *i*th bin is given by the Poisson distribution:

$$p(N_i|\mu_i) = \frac{1}{N_i}\mu_i^{N_i}\,\mathrm{e}^{-\mu_i}, \tag{35}$$

where the mean $\boldsymbol{\mu} \equiv \langle\boldsymbol{N}\rangle$ is the average over an ensemble of realizations. Fluctuations in the counts are larger for point processes that display spatial clustering. In this case the covariance matrix of the binned counts can be written as (Lima & Hu 2004)

$$\Sigma^{\rm counts}_{ij} = S_{ij} + M_{ij}, \tag{36}$$

where $\boldsymbol{S}$ denotes the sample covariance encoding information from the two-point correlation function, and the second term is the diagonal Poisson noise $M_{ij} = \langle N_i\rangle\delta_{ij}$. Hu & Kravtsov (2003) have shown that the sample covariance is subdominant with respect to Poisson errors when a cluster survey encompasses a large fraction of the sky, covers a broad redshift interval and high-threshold masses are adopted. We therefore neglect it in our calculations as we will treat

clustering separately as described in the next section. Note that this is different from considering a count-in-cells experiment where the covariance of the counts is a direct observable (Oguri 2009; Cunha et al. 2010). For negligible sample covariance, the Fisher matrix for the cluster counts can be written as

$$F_{\alpha\beta}^{\rm counts} = \frac{1}{2}{\rm Tr}[\boldsymbol{\Sigma}_{\rm counts}^{-1}(\boldsymbol{\mu}_{,\alpha}\,\boldsymbol{\mu}^{\rm T}{}_{,\beta} + \boldsymbol{\mu}_{,\beta}\,\boldsymbol{\mu}^{\rm T}{}_{,\alpha})] \tag{37}$$

$$= \langle \boldsymbol{N}\rangle_{,\alpha}^{\rm T}\,\boldsymbol{M}^{-1}\langle \boldsymbol{N}\rangle_{,\beta} \tag{38}$$

$$= \sum_{i}^{\#\rm bins} \frac{\partial\langle N_i\rangle}{\partial\theta_\alpha}\frac{1}{\langle N_i\rangle}\frac{\partial\langle N_i\rangle}{\partial\theta_\beta}\bigg|_{\rm fiducial\ model}. \tag{39}$$

7.3 Two-point clustering

Let us now consider the two-point clustering of the X-ray clusters. Our observables will be the angular cross- and auto-spectra $C_\ell(i,j)$ between clusters binned either in redshift or in photon counts. The measured signal is affected by Poissonian shot noise:

$$\tilde{C}_\ell(i,\,j) = C_\ell(i,\,j) + \frac{1}{N_i}\delta_{ij}, \tag{40}$$

where δ_{ij} denotes the Kronecker delta. The covariance matrix for the angular power spectrum can be written as follows (Hu & Jain 2004; Cohn 2006; Huterer et al. 2006; Yamamoto et al. 2007):

$$\boldsymbol{\Sigma} \equiv {\rm Cov}[\tilde{C}_\ell(i,\,j)\,\tilde{C}_{\ell'}(m,n)] = {\rm Cov}_\ell(ij)(mn)$$
$$= \frac{\delta_{\ell\ell'}}{(2\ell+1)f_{\rm sky}}\left[\tilde{C}_\ell(i,m)\,\tilde{C}_\ell(j,n) + \tilde{C}_\ell(i,n)\,\tilde{C}_\ell(j,m)\right]. \tag{41}$$

The covariance matrix is thus block-diagonal, where the number of blocks is given by the number of multipoles ℓ and where the dimension of every block is given by the number of distinct pairs which can be formed with the adopted number of bins, in redshift or photon counts. Assuming a Gaussian-likelihood function for the underlying density field, i.e. for the spherical coefficients $a_{\ell m}$ which define the angular power spectrum $\langle a_{\ell m}a^*_{\ell' m'}\rangle = C_\ell\,\delta_{\ell\ell'}\,\delta_{mm'}$, we write the 'clustering' Fisher matrix as follows:

$$F_{\alpha\beta}^{\rm clust} = \sum_\ell \sum_{(i,j)(m,n)} \frac{\partial C_\ell(i,\,j)}{\partial\theta_\alpha}\,{\rm Cov}_\ell^{-1}(ij)(mn)\,\frac{\partial C_\ell(m,n)}{\partial\theta_\beta}. \tag{42}$$

8 RESULTS

8.1 Cluster counts

We first assume having no information on the cluster redshifts and study the constraining power of a number-count experiment. The first row in Table 3 summarizes our (optimal) results, obtained with about 20 logarithmically spaced bins in the range $50 \lesssim \eta \lesssim 10^5$ plus one bin extending to infinity: 1σ error bars often exceed the fiducial values of the parameters themselves and are thus of little interest. We only quote errors obtained marginalizing over the entire parameter set. Note that the conditional errors could be as good as $\Delta f_{\rm NL}^{\rm local} = 9$ and $\Delta\sigma_8 \simeq 10^{-4}$. This indicates that covariances among parameters are strong (see Fig. 8, upper-left panel). The most degenerate pairs are $\Omega_{\rm m}$–σ_8, $f_{\rm NL}^{\rm local}$–σ_8, $f_{\rm NL}^{\rm local}$–$\Omega_{\rm m}$, $\beta_{\rm LM}$–$\sigma_{\rm LM}$ and $\alpha_{\rm LM}$–σ_8. It is exactly these covariances that are reduced by optimizing the binning scheme in η, while conditional errors are rather insensitive to it.

Redshift information on the individual clusters must be added if we want to constrain the cosmological model and the physics of the ICM from a number-count experiment with *eROSITA*. We thus study how the 1σ error bars for the various parameters improve with the accuracy of the redshift estimates. For this calculation, binning is implemented both in photon counts and in redshift. We consider ∼20 logarithmically spaced bins in photon counts as detailed earlier, while redshift bins have size $\Delta z(1+z_{\rm bin})$, where Δz is a parameter we vary and $z_{\rm bin}$ is the median redshift in a bin. As soon as some redshift information is available, even as rough as with $\Delta z \sim 0.1$, uncertainties on the parameters shrink by factors of 10 (e.g. for σ_8). This applies to the marginal errors, indicating that redshift information breaks degeneracies. The conditional errors, on the other hand, do not show any dependence on the number and size of the redshift bins. In Table 3 we list the uncertainties that *eROSITA* should be able to place if a redshift binning with $\Delta z \sim 0.05$ is performed, which approximates what could be achieved from photometric estimates ('counts + photo-z').

Spectroscopic-redshift measurements ($\Delta z \sim 0.01$) would result in significantly better constraints (by 30–60 per cent) on parameters like $n_{\rm s}$, h, $\Omega_{\rm b}$, $\alpha_{\rm LM}$ and $\sigma_{\rm LM}$ with respect to what is achievable using photometric redshifts; yet, *eROSITA* counts alone would not improve upon current constraints which have been however obtained by combining different probes. Note that the current constraints on the cosmology sector listed in Table 3 refer to other probes than galaxy clusters, and the ones on the ICM sector are at fixed cosmology. Our results instead have always been obtained after marginalizing over both the cosmology and ICM sectors simultaneously. Therefore, a direct comparison is not completely meaningful and the entries 'current errors' should be simply considered as a reference. Note that, if the luminosity–mass scaling-relation parameters were exactly known, *eROSITA* cluster counts alone would constrain σ_8 and $\Omega_{\rm m}$ down to $\Delta\sigma_8 = 0.017$ (2.1 per cent) and $\Delta\Omega_{\rm m} = 0.0086$ (3.1 per cent; see Table B1 in Appendix B).

Finally, it is worth stressing that, even with some redshift information, errors in parameter estimates display strong correlations. As shown in the upper-right panel of Fig. 8 (for photo-z bins and a few tens of bins in photon counts), this is particularly evident for the triplet $n_{\rm s}$, h and $f_{\rm NL}^{\rm local}$ within the cosmology sector, all the LM parameters among themselves, and for σ_8 with all the LM parameters (see also Appendix A).

8.2 Angular clustering

8.2.1 C_ℓ without redshift information

Starting from the reference configuration summarized in Table 1, we want to optimize the measurement of the cluster two-point function to extract maximal information, for the all-sky survey and with multipoles in the range $5 \le \ell \le 96$. We start by assuming no knowledge about the redshifts of the individual clusters. The detected clusters will be binned only in terms of the observed photon counts, such that an approximately equal number of clusters are assigned to each bin. Distinguishing in photon counts is fundamental to tighten the error bars both on $f_{\rm NL}^{\rm local}$ and all the other parameters. The gain on $f_{\rm NL}^{\rm local}$ due to the increment in the number of bins already converges after six bins: in fact, shot noise is not negligible already with a few 10^4 objects per bin. The best constraints from the angular clustering are summarized in Table 3, where we report the results obtained using 12 bins ('angular clustering'); while the conditional error on $f_{\rm NL}^{\rm local}$ could be as good as $\Delta f_{\rm NL}^{\rm local} \sim 24$, the rather poor constraints on the other parameters increase the corresponding marginal constraint to ± 46 at 1σ. Not surprisingly, the non-Gaussianity parameter presents very weak correlations with

Table 3. Marginal 1σ errors for the cosmological and the LM parameters obtained using the Fisher-matrix formalism. The label '+ Priors' indicates results obtained adopting external priors on h and Ω_b as detailed in Section 8.4. The row in boldface marks the best constraints obtained using *eROSITA* data only. We refer to the following survey: $T_{exp} = 1.6$ ks, $\eta_{min} = 50, M_{min} = 5 \times 10^{13}\, h^{-1}\, M_\odot, f_{sky} = 0.658, \Delta z = 0.05$.

eROSITA data	FoM	Δf_{NL}^{local}	$\Delta\sigma_8$	$\Delta\Omega_m$	Δn_s	Δh	$\Delta\Omega_b$	$\Delta\alpha_{LM}$	$\Delta\gamma_{LM}$	$\Delta\beta_{LM}$	$\Delta\sigma_{LM}$
Counts	1.1	$\sim 9 \times 10^3$	$\sim$1.6	$\sim$0.5	$\sim$4	$\sim$4	$\sim$0.3	$\sim$1.8	$\sim$7	$\sim$9	$\sim$3
Counts + Priors	4.6	$\sim 8 \times 10^3$	$\sim$1.5	$\sim$0.4	$\sim$2	0.080	0.0113	$\sim$1.7	$\sim$7	$\sim$7	$\sim$2
Counts + Photo-z	10.7	423	0.113	0.0191	0.559	0.558	0.0649	0.20	0.75	$\sim$1	0.277
Counts + Photo-z + Priors	12.8	360	0.100	0.0188	0.205	0.078	0.0110	0.16	0.73	$\sim$1	0.202
Angular clustering	7.1	46	0.257	0.0817	0.845	$\sim$1	0.0974	0.47	$\sim$1	$\sim$3	$\sim$1
Angular clustering + Priors	9.1	42	0.226	0.0693	0.256	0.068	0.0100	0.36	$\sim$1	$\sim$3	$\sim$1
Angular clustering + Photo-z	12.0	10.1	0.097	0.0393	0.264	0.299	0.0232	0.12	0.47	$\sim$1	0.247
Angular clustering + Photo-z + Priors	13.2	9.8	0.095	0.0207	0.076	0.028	0.0033	0.08	0.43	$\sim$1	0.242
Counts + Angular clustering	10.6	42	0.180	0.0582	0.530	0.967	0.0736	0.24	$\sim$1	$\sim$2	0.621
Counts + Angular clustering + Priors	12.5	37	0.169	0.0531	0.154	0.064	0.0089	0.22	$\sim$1	$\sim$2	0.557
Counts + Angular clustering + Photo-z	**16.3**	**8.8**	**0.036**	**0.0118**	**0.088**	**0.153**	**0.0114**	**0.05**	**0.20**	**0.397**	**0.117**
Counts + Angular clustering + Photo-z + Priors	17.2	8.2	0.036	0.0111	0.033	0.027	0.0030	0.05	0.20	0.384	0.114
Counts + Angular clustering + LM fixed	–	36	0.016	0.0099	0.172	0.461	0.0464	–	–	–	–
Counts + Angular clustering + Photo-z + LM fixed	–	8.4	0.003	0.0029	0.055	0.110	0.0092	–	–	–	–
Counts + Angular clustering + *Planck*	19.7	26	0.022	0.0065	0.004	0.005	0.0005	0.04	0.16	0.348	0.137
Counts + Angular clustering + Photo-z + *Planck*	22.1	6.9	0.014	0.0039	0.003	0.003	0.0003	0.02	0.07	0.173	0.045
Current errors[a]	–	[−10,+74]	0.024	0.0061	0.012	0.014	0.0016	0.14	0.42	0.085	0.039
Planck errors[b]	–	–	0.024	0.0071	0.004	0.006	0.0006	–	–	–	–

[a] *WMAP*7+BAO+SN for the cosmology sector independent of the ICM sector, Komatsu et al. (2011); results by Vikhlinin et al. (2009a) for the LM parameters, at fixed cosmology. 95.4 per cent CI for f_{NL}^{local}.
[b] Error estimates for future power-spectrum measurements with *Planck*; marginalization solely over the cosmology sector, excluding f_{NL}^{local}.

the other ones, once a few bins in photon counts are considered. On the other hand, the pairs n_s–h and h–Ω_b are extremely correlated even with the tightest binning scheme (see Fig. 8, centre-left panel). Moreover the measurement of the angular power spectrum in a single redshift bin cannot break the severe degeneracies which plague the ICM parameters, as predictable by simple inspection of Fig. 6 (see also Appendix A).

Note that the minimum multipole which is considered in the analysis of the angular power spectrum impacts the estimation of the different cosmological parameters (Fig. 9, where the effect of ℓ_{max} is also shown). After marginalizing over the whole set of parameters (and considering multipoles up to $\ell_{max} = 96$), the uncertainty on f_{NL}^{local} improves by a factor of 6 if the minimum multipole is reduced from $\ell \sim 20$ to $\ell \sim 5$. On the other hand, the constraints on the other cosmological parameters are insensitive to ℓ_{min}.

8.2.2 C_ℓ tomography

How much does the constraining power of C_ℓ measurements improve if the redshifts of the clusters were available? To answer this question, we divide the *eROSITA* sample into redshift bins of size $\Delta z(1 + z_{bin})$ and, additionally, into 12 bins based on the photon counts. In the rest of the paper, we will refer to this configuration as 'tomography'. By slicing in redshift, the marginal error bars of all parameters drop significantly, even by orders of magnitude. Four are the factors which make the tomography more powerful than measuring C_ℓ from the full sample: (i) the maximum multipole can be raised to much higher values, reaching $\ell_{max} > 200$ for redshift bins above $z \sim 0.8$ with $k_{max} = 0.1\, h\, Mpc^{-1}$; (ii) the C_ℓ signal itself increases for thinner bins due to reduced projection effects; (iii) the scale-dependent bias induced by f_{NL}^{local} is more pronounced at high redshift and not averaged out by the populations of lower redshift less-biased objects; (iv) since we always consider all cross-spectra among different redshift slices, the number of data points scales as $n(n + 1)/2$, n being the number of redshift slices. The proper inclusion of all the cross-spectra (with respect to the case where only auto-spectra are included) tightens the error budget up to 33 per cent (for f_{NL}^{local}) when $\Delta z \sim 0.05$ and up to 40–60 per cent (for f_{NL}^{local}, n_s, h, Ω_b) when $\Delta z \sim 0.01$. Note that even with $\Delta z \sim 0.01$, there are still more than 1000 objects per z-slice in half of the bins.

By combining the angular clustering signal from more than 10 different redshift slices ($\Delta z \sim 0.1$), it is possible to constrain primordial non-Gaussianity of the local type with a marginal error $\lesssim 10$ (the corresponding conditional error on the other hand is $\sim$5–6 at 1σ). On the other hand, the gain in the information about f_{NL}^{local} by increasing the number of redshift slices flattens much faster than almost any other parameter (see also Section 9.4 and Table 5). In Table 3 we give as a reference the constraints obtained with $\Delta z \sim 0.05$ ('angular clustering + photo-z'), consistently with what we adopted for the number-count experiment when photometric-redshift estimates are available. For f_{NL}^{local}, we find a forecasted marginal error of $\sim$10 which is very interesting and could potentially rule out entire classes of inflationary mechanisms. With an exposure of 1.6 ks, a tomography experiment is more efficient than a 'counts + photo-z' measurement to constrain the LM parameters, but we have noticed that the situation is reversed for higher exposure times (i.e. 3 ks). On the other hand, *eROSITA* tomography alone cannot place constraints on the other cosmological and ICM parameters which are by any means competitive to what is already known nowadays by the combination of CMB, BAO and SN data. Note, however, that assuming perfect knowledge of the luminosity–mass relation, the constraints imposed on f_{NL}^{local}, σ_8 and Ω_m by the *eROSITA* tomography alone would be competitive with the current ones (see Table B1 in Appendix B). If vice versa one could assume perfect knowledge of the cosmological parameters, tomography alone would largely improve our knowledge on the slope and evolution of the LM

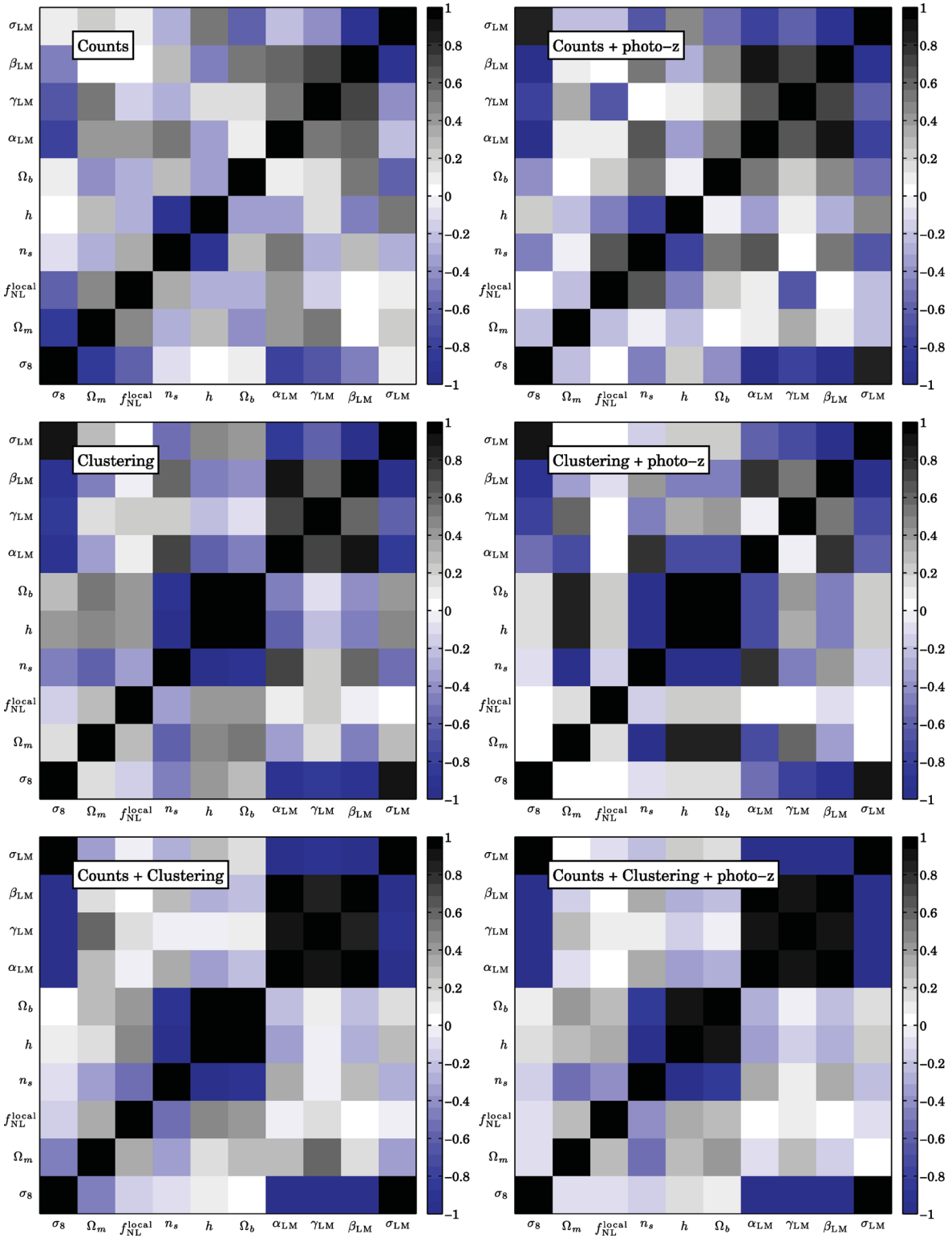

Figure 8. Correlation coefficient between pairs of model parameters for the different experiments.

relation (see in Table 3 the results with *Planck* priors for an upper limit of the uncertainties).

It is worth mentioning that estimates on $f_{\rm NL}^{\rm local}$ based on the C_ℓ tomography are nearly perfectly uncorrelated from any other model parameter (Fig. 8, centre-right panel) although strong correlations are still present in the complementary parameter space.

Fig. 10 allows us to stress the importance of high-redshift objects: there we show how the total FoM [as defined in equation (34) and which takes into account the error bars and correlations among the whole set of 10 parameters] and the marginal constraints on $f_{\rm NL}^{\rm local}$ depend on the individual z-bin, within our binning scheme; the magenta horizontal line refers to the marginal constraint on $f_{\rm NL}^{\rm local}$

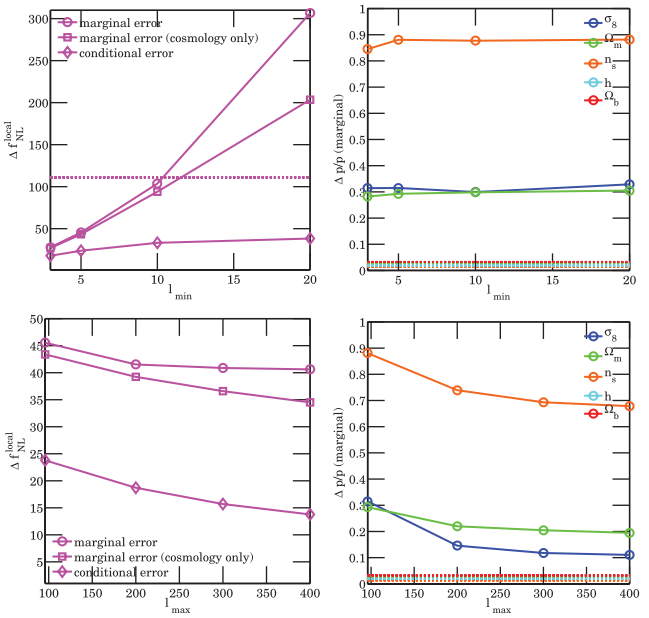

Figure 9. Choice of ℓ_{min} and ℓ_{max} in the clustering measurements: 1σ errors on the different parameters are shown as a function of ℓ_{min} (at fixed $\ell_{max} = 96$, upper panels) and as a function of ℓ_{max} (at fixed $\ell_{min} = 5$, lower panels). The entire *eROSITA* sample is projected on the same sphere and split in 12 bins based on the photon counts η.

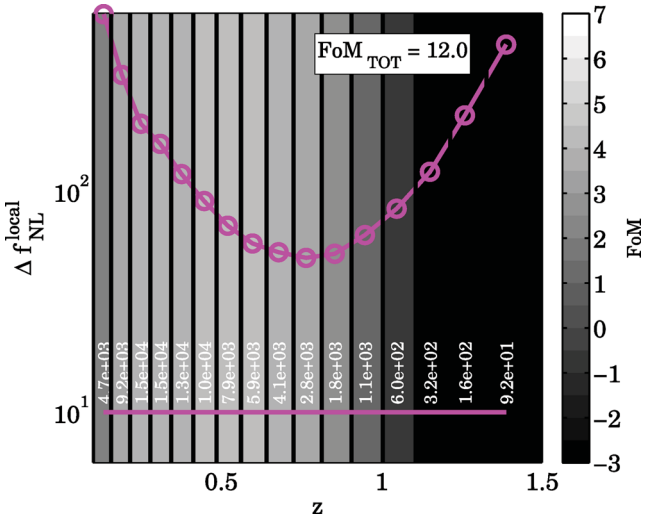

Figure 10. Marginal error on f_{NL}^{local} and total FoM from different individual redshift bins. The bin width is $\Delta z(1 + z)$ with $\Delta z = 0.05$ for a total of 16 bins up to $z \simeq 1.5$. Magenta circles indicate the constraints on f_{NL}^{local} obtained from every individual redshift slice, the horizontal magenta line is the global constraint on f_{NL}^{local} obtained considering all the bins together, including cross-correlations among redshift bins. The FoM of equation (34) is colour-coded in shades of grey for the individual z-bins, while the total FoM of the tomographic measurement is indicated in the upper-right box.

given by the combination of all redshift slices, including cross-correlation among bins; also the number of objects in each redshift bin is indicated. The final constraints are the results of at least three factors: the thickness and the redshift of the z-bin, and the number of objects in each bin. Considering only the slice with $0.76 < z < 0.85$ (which contains ∼2800 clusters) gives already $\Delta f_{NL}^{local} = 51$. In general, the sample of clusters with $z > z_{med}$ better constrains the cosmological parameters (by a factor of a few) with respect to the identically sized sample with $z < z_{med}$.

8.3 Combining counts and clustering

We want now to combine our results on the cluster counts and on the angular power spectrum to get tighter constraints on the model parameters. This requires accounting for the cross-covariance between the two probes, which is proportional to the angular bispectrum of the clusters (see e.g. Takada & Bridle 2007). For Gaussian initial conditions, the bispectrum vanishes on large scales. Cross-covariances remain small also for the weakly non-Gaussian models we consider, in spite of the large cluster bias factors. This is because we only consider very large scales and rather heavily projected data. For this reason we ignore cross-covariances between the cluster number counts and the measurement of the angular power spectrum. As a result, the total Fisher matrix is obtained by summing up the single Fisher matrices of the individual experiments. The results obtained considering the joint data sets are summarized in Table 3, in Fig. 11, where error contours for a selection of parameter pairs are shown, and in Fig. 8 where we quantify the correlations among parameter pairs for all the different probes. Once again, we distinguish the cases in which redshift estimates for the individual clusters are available or not. For all parameters, measuring photometric redshifts (with $\Delta z \sim 0.05$) shrinks the marginal error bars by a factor of 4 or 5. Adding information on the number counts to tomographic C_ℓ measurements has little impact on f_{NL}^{local}, but significantly shrinks the confidence interval of the other cosmological and ICM parameters. On the other hand, 'counts + photo-z' alone gives better results than 'counts + angular clustering' without photo-z for all parameters but f_{NL}^{local} and n_s. Properly taking into account the uncertainties on the LM parameters strongly degrades the cosmological constraints which could be ideally achieved if the cluster observable–mass mapping was perfectly known (e.g. 'counts + angular clustering + photo-z' versus 'counts + angular clustering + photo-z + LM fixed', and Table B1).

8.4 Adding external priors

X-ray cluster counts and power spectra (with and without photometric redshifts) cannot simultaneously determine *all* the model parameters (see Table 3 and Fig. 11); in particular, the triplet n_s, h and Ω_b are left unconstrained by *eROSITA* data. We therefore complement *eROSITA* with strong standard priors on the Hubble parameter (from the Hubble Key Project, $\Delta h = 0.08$; Freedman et al. 2001) and on the mean baryon density of the universe (from primordial nucleosynthesis, $\Delta(\Omega_b h^2) = 0.002$; Kirkman et al. 2003), as commonly done in X-ray studies (e.g. Mantz et al. 2010b). The sensitivity of our results to these priors is shown in Table 3 ('+ Priors '). The parameter that benefits the most is the spectral index, while all the other cosmological and ICM parameters are rather insensitive to them (at least for the joint constraints with photo-z). While constraints on h and Ω_b are dominated by the imposed priors for the abundance experiments and the clustering without redshifts, *eROSITA*'s tomography (and thus the combinations of the experiments) significantly contributes to further shrink those errors.

We focus now on the CMB analysis performed by the *Planck* satellite whose results will be available by the time the *eROSITA* all-sky survey will be completed. We consider the *Planck* Fisher matrix for a measurement of the power spectrum of temperature anisotropies calculated by the Dark Energy Task Force (Albrecht et al. 2009), kindly made available to us by Dragan Huterer and

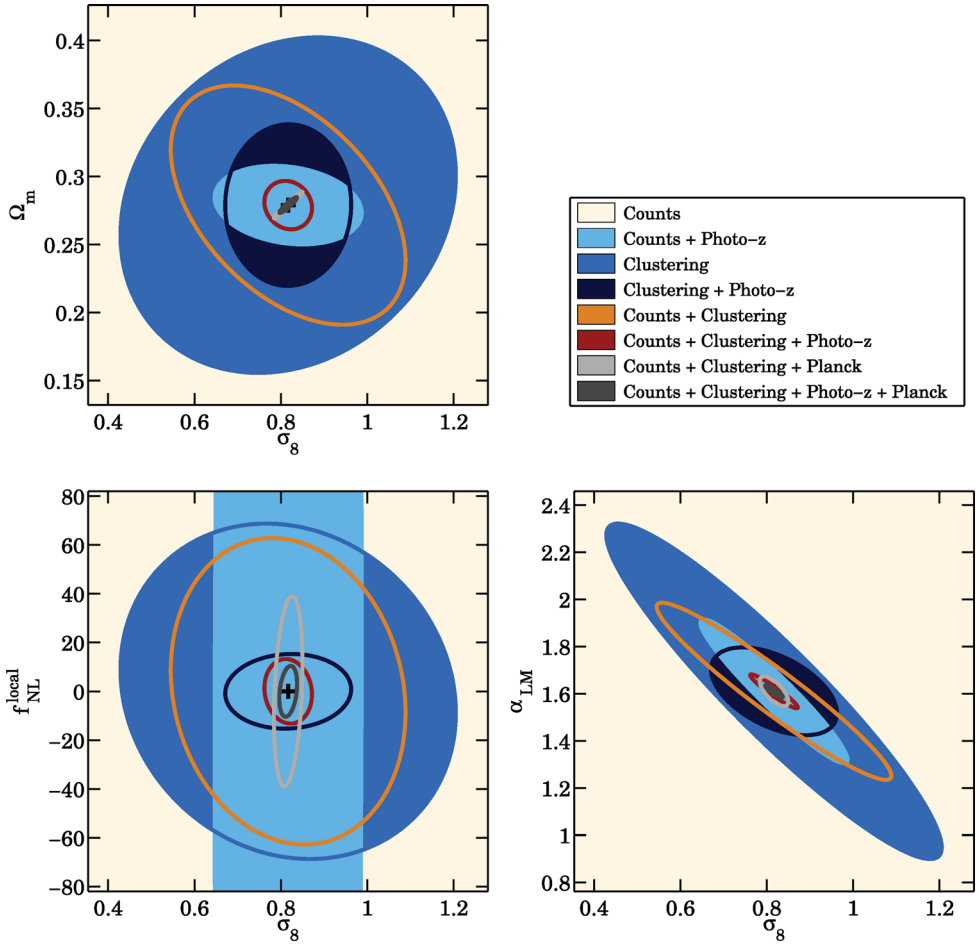

Figure 11. Joint 1σ error ellipses for a selection of parameter pairs obtained by marginalizing over all the other model parameters (no priors assumed). Individual experiments and their combinations for the all-sky survey (described in Table 1) are indicated with different colours. Contours for the number-count experiment with no redshift information vastly exceed the area in the plot. The complete set of error ellipses is given in Appendix A, with priors oh h and Ω_b.

Wayne Hu. This constrains all cosmological parameters but f_{NL}^{local} (we do not consider the CMB bispectrum in this work). The results obtained using the *Planck* forecast as a prior for our *eROSITA* analysis are shown in Table 3; the constraints on all parameters are strongly improved, in particular for n_s, h, Ω_b (where the improvement reaches a factor of 30!). Yet, *eROSITA* significantly contributes to the determination of all parameters. Cosmological constraints on σ_8 (which is not a 'natural' choice to fit CMB data) and Ω_m will be known at ∼1.5–2 per cent accuracy, while constraints such as $\Delta f_{NL}^{local} \sim 7$ will be comparable to the results of the CMB three-point statistics (but on different spatial scales). Similarly, all the ICM parameters will be more accurately determined than they are nowadays (see error ellipses in Figs A1, A2 and A3). Note that in terms of LM parameters only, adding *Planck* priors to the cosmological sector ('counts + angular clustering + *Planck*') is almost equivalent to measuring photometric redshifts for the whole cluster sample ('counts + angular clustering + photo-z'). A comparison between the constraining capabilities of *Planck* and *eROSITA* is given in Table B2 in Appendix B, where the analysis is repeated exclusively for the cosmology sector and assuming Gaussian initial conditions (five-parameter fit). Note that, if we could perfectly characterize the X-ray cluster scaling relations, *eROSITA* would outperform *Planck* in the determination of σ_8, while, even in this idealistic scenario, *Planck* would still do significantly better for n_s, h and Ω_b.

9 DISCUSSION

9.1 Wide or deep surveys?

Is there any advantage in undertaking a deeper survey than the all-sky one analysed so far? We consider here an hypothetical survey with average exposure time of 7.5 ks. Accordingly, we assume a sky coverage of 6000 deg^2 (with $\ell_{min} \sim 9$), which gives approximately the same amount of observing time used for the all-sky survey. Although the higher exposure time enables the detection of fainter clusters at high redshift, the limited sky coverage significantly reduces the total number of sources. With a detection limit of 50 photons and a minimum mass of $5 \times 10^{13}\, h^{-1}\, M_\odot$, the deeper and less extended survey should identify 6.85×10^4 clusters with a median redshift of 0.56.

These changes impact the cosmological constraints in different ways. For a number-count experiment, the deeper survey better constrains some parameters such as f_{NL}^{local}, n_s and γ_{LM} (15–30 per cent improvements), but is not optimal overall. On the other hand, clustering studies clearly benefit from the all-sky coverage (parameter constraints improve by many tens per cent), especially if one wants to measure f_{NL}^{local} through the scale-dependent bias which is only evident on large projected angular scales. In Table 4, we report the total number of detected clusters and some constraints on the model parameters that can be obtained from the joint analysis of

Table 4. Forecasted performance of different survey strategies (no priors assumed). The reference case (labelled *eROSITA*) refers to the all-sky survey extensively discussed in Table 3. In all cases, we consider a detection limit of 50 photons and a minimum cluster mass of $5 \times 10^{13}\ h^{-1}\,\mathrm{M}_{\odot}$. Results are given for the joint analysis of number counts and angular clustering with photometrically determined cluster redshifts, i.e. the data are split in redshift bins of width $0.05(1+z)$. We use here separate figures of merit to distinguish the cosmological parameters from those of the LM relation.

Surveys	Area (deg^2)	$T_{\rm exp}$(ks)	$N_{\rm objects}$	$\Delta f_{\rm NL}^{\rm local}$	FoM$^{\rm Cosmo}$	FoM$^{\rm ICM}$
eROSITA	27 000	1.6	9.32×10^4	8.8	8.0	5.3
Deeper *eROSITA*	27 000	3.0	1.61×10^5	6.5	8.6	5.6
Focused *eROSITA*	6000	7.5	6.85×10^4	21.1	6.4	4.3
1/2 *eROSITA*	13 500	1.6	4.66×10^4	18.9	6.5	4.6
(1/2 + 1/2) *eROSITA*	27 000	1.6	9.32×10^4	13.4	7.3	5.1
$z \leq 1$ *eROSITA*	27 000	1.6	9.19×10^4	9.5	7.8	5.2
'The magnificent 1000'	27 000	1.6	$\sim$1000	41	2.0	1.1

cluster counts and C_ℓ tomography (both with redshifts of photometric quality) for a series of survey strategies, where the covered sky fraction and the average exposure time are changed with respect to our reference choice. For example, the 3-ks survey over 27 000 deg^2 could be realized if, instead of performing 3 years of pointed observations after the first 4 years of the *eROSITA* mission, the all-sky survey would be continued for the remaining lifetime of the satellite. This, of course, would have the drawback that the planned pointed cluster follow-up observations could not be performed. The mild improvement in the resulting constraints might not justify this possible extension of the all-sky survey.

9.2 Does 1/2+1/2 equal 1?

It has been agreed that *eROSITA* data will be equally split between the Russian and the German consortia; each of them will own an equal fraction of the sky. We want to investigate what would be the impact of performing separate analyses for the two half-sky surveys. Two effects have to be considered: halving the number of objects and the loss of the largest angular spatial separations where the effect of primordial non-Gaussianity is larger. As an example, we report how passing from $f_{\rm sky} = 0.658$ to 0.33 (with $\ell_{\rm min} \sim 7$) impacts the constraints on $f_{\rm NL}^{\rm local}$ and σ_8. We find that the joint marginal errors for the all-sky survey $\Delta f_{\rm NL}^{\rm local} = 8.8$ and $\Delta\sigma_8 = 0.036$ degrade to $\Delta f_{\rm NL}^{\rm local} = 18.9$ and $\Delta\sigma_8 = 0.062$. Combining the results from the two halves of the sky a posteriori would then give $\Delta f_{\rm NL}^{\rm local} = 13.4$ and $\Delta\sigma_8 = 0.044$ (where we have optimistically assumed that the two halves of the sky are statistically independent).

9.3 The case with no clusters beyond $z \sim 1$ and 'the magnificent 1000'

Many parameters of interest exhibit stronger effects on the cluster number counts and C_ℓ at higher redshifts than at lower redshifts; this is particularly pronounced for $f_{\rm NL}^{\rm local}$, but also evident for some of the ICM parameters. Measurements at high redshifts may be difficult or even out of reach for at least two reasons: (i) the higher the redshift, the more problematic the active galactic nucleus contamination might be; (ii) the higher the redshift, the lower the chances of successfully measuring a (photometric or spectroscopic) redshift are. We briefly compare here the results discussed so far with the pessimistic scenario where no clusters beyond redshift $z \sim 1$ can be included in the analysis. The total number of objects which would be lost beyond redshift 1 is about 1200 (for $T_{\rm exp} = 1.6$ ks; three times higher with a double exposure time). With redshift bins of width $0.05(1+z)$, the constraints on $f_{\rm NL}^{\rm local}$ would deteriorate to $\Delta f_{\rm NL}^{\rm local} = 517$ and 11.1 for a number-count and a tomography experiment, respectively (see also Table 4 for the joint constraint). Similarly, the loss of accuracy in measuring all the other parameters would be more pronounced for number counts, with relative deteriorations of about 10–20 per cent.

Let us now imagine to only use the most massive 1000 clusters at $z \geq 1$ for our analysis ('the magnificent 1000'). This sample includes objects with masses above $\sim 2.2 \times 10^{14}\ h^{-1}\,\mathrm{M}_{\odot}$, possibly similar to what Sunyaev–Zel'dovich surveys might yield in the future. The joint analysis of number counts and C_ℓ tomography with this subsample would give a marginal error of $\Delta f_{\rm NL}^{\rm local} \sim 41$ (with photometric-redshift information). The attractive conditional error of $\Delta f_{\rm NL}^{\rm local} \sim 12$ is in practice uninteresting because plagued by huge systematics and parameter degeneracies; with the 'magnificent 1000' only the exponential cut-off of the mass function is probed, where the models are more uncertain and where every parameter is in practice degenerate with another. Note that for the analysis with the whole *eROSITA* sample, the comparison between conditional and marginal error is much less dramatic, reading $\Delta f_{\rm NL}^{\rm local} \sim 4.4$ versus $\Delta f_{\rm NL}^{\rm local} \sim 8.8$ (see Table 3). In any case, the marginal constraints on all the other parameters would be much less appealing (Table 4). Combining the analysis of the magnificent 1000 with *Planck* priors would still give $\Delta f_{\rm NL}^{\rm local} \sim 26$ and $\Delta\sigma_8 = 0.024$ (corresponding to a relative error of 2.9 per cent), a figure which is destined to further improve with multiwavelength follow-ups of the cluster sample and consequently better mass proxy measurements.

9.4 Spectroscopic redshifts

Our reference forecasts assume that photometric redshifts of the individual clusters will become available. However, given that spectroscopic follow-ups of the *eROSITA* survey are being proposed, in Table 5 we present new results that refer to the optimistic scenario where spectroscopic redshifts for all the detected clusters will be available. In this case we use redshift bins of thickness $0.01(1+z)$. For all model parameters, improvements are much more pronounced for the C_ℓ tomography rather than in a count experiment. Marginal constraints on all the cosmological parameters but $f_{\rm NL}^{\rm local}$ and σ_8 exhibit an improvement of more than 50 per cent when passing from photometric- to spectroscopic-redshift quality with a tomography measurement alone; all parameters but $f_{\rm NL}^{\rm local}$ get constrained 30–40 per cent tighter when joint constraints with spectroscopic redshifts are considered with respect to the photo-z case. Overall,

Table 5. Forecasted total FoM and 1σ marginal errors on $f_{\rm NL}^{\rm local}$ and σ_8 obtained with the *eROSITA* cluster sample. First, no redshift information is assumed. Then the data are sliced in redshift bins of width $\Delta z(1+z)$, with $\Delta z = 0.05$ and 0.01 (mimicking photometric versus spectroscopic redshift estimates). No priors assumed.

eROSITA data	FoM	$\Delta f_{\rm NL}^{\rm local}$	$\Delta\sigma_8$
Counts	1.1	$\sim 9 \times 10^3$	~ 1.6
Counts + Photo-z	10.7	423	0.113
Counts + Spectro-z	11.2	370	0.095
Angular clustering	7.1	46	0.257
Angular clustering + Photo-z	12.0	10.1	0.097
Angular clustering + Spectro-z	14.5	7.8	0.059
Counts + Angular clustering	10.6	42	0.180
Counts + Angular clustering + Photo-z	16.3	8.8	0.036
Counts + Angular clustering + Spectro-z	17.7	7.0	0.024

the total FoM would improve substantially if spectroscopic redshifts were available.

9.5 The mass cut

So far, we have always applied a cut in the η–z plane which corresponds to a cluster mass of $M = 5 \times 10^{13}\, h^{-1}\,{\rm M}_\odot$ in the fiducial model. Moving this threshold significantly changes the selected cluster population both in terms of their sheer numbers and redshift distribution (see Table 2, for details). Of course, there are more objects when the mass threshold is lowered and this formally produces better parameter constraints from counting experiments. On the other hand, a lower threshold reduces the effective bias of the cluster population (and thus the non-Gaussian correction) and moves also down the median redshift (and thus $\ell_{\rm max}$ for the clustering measurement): for the clustering experiments, trends are different for different parameters. The joint constraints for $f_{\rm NL}^{\rm local}$ are rather insensitive to the mass threshold, while the parameters which are most affected by the exact value of the mass cut are σ_8 and $\gamma_{\rm LM}$ (their constraints improve by 30 per cent when $M_{\rm cut} = 10^{13}\, h^{-1}\,{\rm M}_\odot$).

A note of a caution is in order here. In a meaningful Fisher-matrix study, the sample definition (and thus the mass cut) must not change with the model parameters. We identify the locus in the η–z which corresponds to a cluster with the threshold mass in the fiducial model and never modify it when we compute the derivatives with respect to the parameters. This mimics what would be done in practice to select high-mass objects out of an observational sample. The sample selection is done before computing the statistical quantities. For this reason, it would be incorrect to impose a cut based on the actual mass or X-ray luminosity of the clusters as sometimes it has been done in the literature (unless mass or luminosity is a direct observable, which is not the case for *eROSITA*). We have checked that adopting this procedure leads to unrealistically optimistic forecasts.

10 OTHER NON-GAUSSIAN MODELS

Primordial non-Gaussianity of the local type is only one (the simplest) of the countless ways to perturb the primordial gravitational potential around the Gaussian assumption (e.g Chen 2010). Here we present the error budget that *eROSITA* should achieve shall the data be fitted with two other models/templates for early non-Gaussianity, the so-called orthogonal and equilateral types. These models differ from the local one in the sense that the bispectrum of the Bardeen's potential peaks at different triangle configurations and are characterized by a single parameter, $f_{\rm NL}^{\rm ortho}$ or $f_{\rm NL}^{\rm equi}$, which quantifies the amplitude of such bispectrum (Creminelli et al. 2006; Senatore, Smith & Zaldarriaga 2010). While the local shape is expected in all models where non-linearities develop outside the horizon (e.g. in multifield inflation), equilateral non-Gaussianity is produced in single-field inflationary models with a non-minimal Lagrangian where the mode coupling is created by non-canonical kinetic terms or higher derivative operators (e.g. in ghost inflation or Dirac-Born-Infeld (DBI) inflation). Finally, the orthogonal template reproduces (among the others) non-Gaussian features arising from assuming non-standard vacuum choices. These three shapes are 'orthogonal' to each other (Babich, Creminelli & Zaldarriaga 2004; Senatore et al. 2010) and linear combinations of them can arise in physically motivated models of the early universe.

In terms of late-time observables, the striking difference between these models lies in the scale-dependence of the bias for DM haloes: at large separations, the bias scales as $f_{\rm NL}^{\rm local}\, k^{-2}$ and $f_{\rm NL}^{\rm ortho} k^{-1}$ for the local and the orthogonal types respectively, while it is asymptotically constant (but, for fixed halo mass, numerically different from that in the Gaussian case) for the equilateral model. The different shapes of the primordial bispectra imply differences in the skewness of the linear density field and, consequently, different modifications to the Gaussian halo mass function too, via equations (8) and (9). We adopt the formulae for the skewness from Taruya, Koyama & Matsubara (2008) and Schmidt & Kamionkowski (2010), and the improved formulae for the non-Gaussian halo bias by Desjacques, Jeong & Schmidt (2011); these have shown better agreement with N-body simulations than previous analytical derivations. However, these expressions are only valid asymptotically as $k \to 0$ and cannot be used at much larger k where the halo bias is basically constant and the provided formulae do not reproduce such behaviour. In order to solve this problem, we have manually imposed this asymptotic behaviour for large k by removing the scale dependencies due to the linear transfer function $T(k)$ at the wavenumbers where the factor $1/T(k)$ starts to dominate.

As detailed in Table 6, given the less prominent scale-dependence of the halo bias, the constraints on $f_{\rm NL}^{\rm ortho}$ and $f_{\rm NL}^{\rm equil}$ are weaker than for the local case; the constraints on the other cosmological parameters and those for the LM relation also exhibit a non-negligible modification. Counts and tomography joint constraints read 0.053 and 0.049 for σ_8 in the orthogonal and equilateral models, respectively, instead of 0.036 with the local template. LM parameters worsen by 10–20 per cent and 20–40 per cent with the orthogonal and equilateral models, respectively, while the triplet $n_{\rm s}, h, \Omega_{\rm b}$ improve in both cases by a few per cent.

11 ADDITIONAL REMARKS

In this section, we critically discuss some of the assumptions and the methods we have been using to derive our main results.

11.1 Theoretical models for the halo mass function

Since the parameters of the mass function are determined from N-body simulations, they are known with some intrinsic uncertainty that we have ignored in our main study. One possible way of gauging this uncertainty is to introduce in the Fisher-matrix analysis a set of nuisance parameters (as many as the mass-function parameters) with their own prior distribution (which embodies the covariance matrix from the fits to the simulation) and marginalize over them

Table 6. Marginal 1σ constraints enabled by *eROSITA* for different models of primordial non-Gaussianity. Assumptions and the survey strategy are as in Table 3 with no external priors unless explicitly stated.

eROSITA data	$\Delta f_{\rm NL}^{\rm local}$	$\Delta f_{\rm NL}^{\rm ortho}$	$\Delta f_{\rm NL}^{\rm equil}$
Counts	9×10^3	4×10^4	2×10^4
Counts + Photo-z	423	2×10^3	1×10^3
Angular clustering	46	461	1.4×10^3
Angular clustering + Photo-z	10.1	102	1.3×10^3
Counts + Angular clustering	42	317	1.1×10^3
Counts + Angular clustering + Photo-z	8.8	36	144
Counts + Angular clustering + *Planck*	26	168	740
Counts + Angular clustering + Photo-z + *Planck*	6.9	19	115
*WMAP*7, 95 per cent CI Komatsu et al. (2011)	$[-10, +74]$	$[-410, +6]$	$[-214, +266]$

(see Cunha & Evrard 2010; Wu, Zentner & Wechsler 2010, for dark-energy surveys). We have implemented this scheme and repeated our calculations using the covariance matrices for the parameters $A_0^{\rm TMF}$, $a_0^{\rm TMF}$, $b_0^{\rm TMF}$ and $c_0^{\rm TMF}$ kindly made available to us by Jeremy Tinker. Unfortunately, owing to the procedure used to fit the simulations, a covariance matrix including also the three evolutionary parameters $A_z^{\rm TMF}$, $a_z^{\rm TMF}$ and α is not available. Anyway, our analysis should at least give an order-of-magnitude estimate of the effect. The errors provided by Jeremy Tinker on his $z = 0$ mass function parameters at fixed cosmology translate in an overall uncertainty of 1 per cent in the shape of the mass function; it is the variation in cosmology which is responsible for the 5 per cent accuracy level quoted in Tinker et al. (2008). In order to approximately take into account possible larger uncertainties, we have rescaled the covariance matrix so that to obtain a marginal uncertainty of about 10 per cent in the abundance of objects with $M \sim 10^{15}\ h^{-1}\,{\rm M}_\odot$ at $z = 0$ before using it as a prior on the mass-function parameters. We find that, within this set-up, the constraints on the parameters both of the cosmology and ICM sector are degraded only by up to 10 per cent when four additional mass function parameters are included in the fitting analysis and marginalized over. These constraints are destined to further degrade when adding the three evolutionary parameters. Moreover, this picture does not take into account possible systematic errors (up to 20 per cent) that baryonic physics seems to induce in the halo mass function (Stanek, Rudd & Evrard 2009; Cui et al. 2011).

Imperfect knowledge on the large-scale bias of the DM haloes should have a smaller effect and will not be discussed here (see Wu et al. 2010).

11.2 Mass–luminosity relation

Our forecasts rely on a series of assumptions for converting DM halo masses into X-ray photon counts.

(1) We have assumed a power-law LM relation. While there is, as of now, no very compelling evidence that this assumption breaks down (see e.g. Sun et al. 2009; Eckmiller et al. 2011), the scatter has been shown to increase for low-mass clusters (Eckmiller et al. 2011). For this reason, we have introduced a minimum mass threshold and varied it within a reasonable range to test the stability of our results.

(2) We have assumed that the scatter around the power-law relation is lognormal, but no consensus has been reached regarding the amplitude and nature of this noise component (see e.g. Pratt et al. 2009; Vikhlinin et al. 2009a; Stanek et al. 2010). As shown by Shaw, Holder & Dudley (2010), an unknown amount of asymmetry in the scatter of the observable–mass relation can affect cosmological constraints in the same manner as additional uncertainties in the fiducial value of the scatter $\sigma_{\rm LM}$ itself.

(3) We have used the current limited knowledge on the LM relation to fix the parameters that define our fiducial model. For instance, we used a scatter in the LM relation of 40 per cent (Vikhlinin et al. 2009a). However, more recent observational scaling relations for core-excised clusters show a reduced dispersion, although spanning somehow smaller redshift ranges (Mantz et al. 2010a). We have repeated our analysis adopting the evolving scaling relations measured by Mantz et al. (2010a), converted in the (0.5–2.0) keV band; we find that the number of clusters detected by *eROSITA* increases by more than 30 per cent, with a total population of 1.24×10^5 objects (more massive than $5 \times 10^{13}\ h^{-1}\,{\rm M}_\odot$) and a slightly lower median redshift, $z_{\rm median} \sim 0.31$. Consequently, the joint constraints on all the cosmological parameters are improved by 10–50 per cent, with the exception of $f_{\rm NL}^{\rm local}$ and $\Omega_{\rm m}$ which show a smaller improvement. On the other hand, the marginal constraints on the LM parameters themselves (but not on the LM scatter) are tighter by a factor of a few. The choice of the fiducial prescription for the LM relation changes more the predictions for the cluster counts than for the clustering measurements, and $f_{\rm NL}^{\rm local}$ is the parameter which exhibits the smallest dependence on it. In any case, also in the light of our (possibly conservative) predictions, one of the major results of this paper is that *eROSITA* and *Planck* results combined together will be able to constrain the slope and the evolution factor of the LM relation at per cent level (see Table 3).

(4) We assumed that the slope and the scatter of the LM relation do not depend on redshift. This is basically Occam's razor applied to current data but might not be adequate for *eROSITA* accuracy.

(5) We always assumed no prior knowledge for the measurements of the ICM parameters which, in our study, are fully determined by *eROSITA* data. Adding priors in fact would require assuming a covariance matrix for the parameters. Results adopting perfect prior knowledge of such parameters are given as a reference in Table B1.

11.3 Temperature–mass relation

Fig. 1 and the discussion of Figs 5 and 6 not only show that the photon counts depend very weakly on the X-ray cluster temperature, but also that the exact TM relation for galaxy clusters has a little effect on our observables. We have checked anyway what happens

if four additional parameters regulating this scaling relation are included in the analysis of Table 3 (10+4 parameter fit). We found that this leads to a deterioration of the constraints in the cosmology sector (by an amount ranging from a few per cent to a factor of a few for $f_{\rm NL}^{\rm local}$) as the new parameters are poorly constrained by the data. It is worthwhile mentioning that the deterioration on the cosmological constraints (six parameters) due to four additional temperature–mass scaling-relation parameters is up to three times less severe than the effect of four additional parameters regulating the LM relation and its redshift evolution (see Appendix B and Table B3).

11.4 Limber approximation

The Limber approximation is often used to forecast the constraining power of the angular power spectrum for tracers of the cosmic large-scale structure. It is well known, however, that this approximation, for Gaussian initial conditions, becomes less and less accurate when projections are taken within thinner and thinner redshift bins (Simon 2007; Loverde & Afshordi 2008). We find that this effect becomes even more important in the presence of primordial non-Gaussianity of the local type or whenever a scale-dependent DM halo bias changes the shape of the angular power spectrum on large scales. With $f_{\rm NL}^{\rm local} \sim 100$, the Limber approximation deviates from the exact calculation by up to 20 per cent for $\ell \sim 5$. Remarkably, the sign of the discrepancy reverts depending on the actual value of $f_{\rm NL}^{\rm local}$ (see also Giannantonio et al. 2011). Therefore, the inaccuracy of the Limber approximation is particularly damaging to compute the Fisher matrix for a clustering experiment where derivatives of C_ℓ with respect to the individual parameters must be taken. We have noticed that using the Limber approximation all over the considered multipole range to predict the performance of a *eROSITA* C_ℓ study can underestimate the marginal error on $f_{\rm NL}^{\rm local}$ by a factor of 4.

11.5 The mildly non-linear regime

As discussed in Section 8.2, the current accuracy to which we model non-linearities both in the matter-density field and in the cluster bias prevents us to trust predictions including information from scales with $k > k_{\rm max} = 0.1\,h\,{\rm Mpc}^{-1}$. We have formally tested that if one could (with more robust models for the mildly non-linear regime) increase this limit to $k_{\rm max} = 0.3\,h\,{\rm Mpc}^{-1}$, the joint *eROSITA* constraints (with photometric redshifts) might tighten by 20–50 per cent for all parameters but $f_{\rm NL}^{\rm local}$.

11.6 Other issues

In our analysis, the cosmology and ICM sectors are not fully independent. In fact, equation (18) introduces a correlation between the LM-evolution parameter and the cosmology sector through the term $\gamma_{\rm LM}\,\ln E(z)$. On the other hand, in Section 11.2, we have presented forecasts based on the alternative LM relation by Mantz et al. (2010a), where the evolution scales as $\gamma_{\rm LM}\,\log_{10}(1+z)$ and does not couple with the cosmological parameters. Also $\Omega_{\rm b}$ should correlate with the LM relation since the cosmic baryon fraction relates to the total gas mass of a cluster and thus to its observed *X*-ray brightness. We postpone to future work the choice of a proper parametrization for this effect.

Throughout our study, we have assumed a detection limit for the galaxy clusters of 50 photon counts, assuming the total flux gets detected. We defer to future work the exploration of different selection criteria, e.g. based on the signal-to-noise ratio. Moreover, we will address the impact of changing the photon-count limit and compare our findings with the output of the *eROSITA* sub-sample with strong observed fluxes (say above 1000 photon counts) and thus better mass proxies than $L_{\rm X}$.

Finally, we have assumed a constant exposure time $T_{\rm exp}$ and a uniform hydrogen column density $N_{\rm H}$, instead of taking into account the possible variations of these quantities across the survey area. A more detailed treatment of the distribution of $T_{\rm exp}$ and $N_{\rm H}$ may introduce corrections to our forecasts: for example, within Sunyaev–Zel'dovich cluster count measurements, Khedekar, Majumdar & Das (2010) have shown that the combination of a wide with a deep survey, keeping fixed the total exposure time, gives better constraints than a longer exposure wide survey only. Further study is required to assess whether this is the case also for X-ray cluster count and clustering experiments, and when fluctuations of $T_{\rm exp}$ and $N_{\rm H}$ along different lines of sight are not averaged over large patches of the sky.

12 CONCLUSIONS AND SUMMARY

We have forecasted the accuracy with which the X-ray telescope *eROSITA* will constrain cosmological parameters based on the number counts and spatial distribution of galaxy clusters. Our reference case considers 10 model parameters, six of which characterize the cosmological model (vanilla, flat, ΛCDM model) while the remaining four describe the luminosity–mass relation for galaxy clusters. Special attention is dedicated to the primordial non-Gaussianity parameter $f_{\rm NL}^{\rm local}$.

Galaxy clusters are sorted in terms of the photon counts that will be detected by the *eROSITA* telescope. We convert the masses of DM haloes (for which we can predict abundance and clustering properties as a function of the cosmological parameters) into this observable by taking into account observationally motivated scaling relations, the properties of the X-ray detector and the integration time of the observations. We find that, in an all-sky survey with a typical exposure time of 1.6 ks, *eROSITA* will observe 9.3×10^4 galaxy clusters (more massive than $5 \times 10^{13}\,h^{-1}\,{\rm M}_\odot$) above the detection limit of 50 photons in the (0.5–2.0) keV band. Their redshift distribution will be broad, extending up to $z \sim 1.5$ with a median of 0.35.

Our forecast is based on measuring the abundance of galaxy clusters as a function of the X-ray photon counts and the corresponding angular power spectra, via a Fisher-matrix approach. We combine the two experiments without assuming any prior knowledge of the X-ray scaling-relation parameters (the so-called self-calibration technique). We distinguish two cases based on whether redshift information on the individual clusters is available or not. Finally, we integrate *eROSITA* data with priors on the Hubble parameter and on the mean baryon fraction, and with future constraints from the *Planck* satellite; we analyse different survey strategies, study the impact of model uncertainties and explore how constraints degrade when extra nuisance parameters are considered. Our main findings are reported in Tables 3, 4, 5 and 6. They can be summarized as follows.

(i) Despite the unprecedented size of the *eROSITA* all-sky sample, without any knowledge of the redshifts of the individual clusters, it is not possible to simultaneously improve currents constraints on cosmology (with the exception of $f_{\rm NL}^{\rm local}$) and on the LM scaling relation. Redshift information is vital to break the strong degeneracies among the parameter estimates. The availability of photometric redshifts, with an accuracy better than $0.05(1+z)$, already shrinks

the constraints on all parameters by a factor of many times (see Table 3).

(ii) Binning the data in X-ray photon counts (η) already removes some degeneracies but, in general, binning in redshift is more efficient in tightening the error bars on the model parameters, although much more expensive in terms of observing time. Anyway, binning in η should be always adopted to achieve the optimal constraints independently of the accuracy to which the cluster redshifts are known.

(iii) A tomographic study of the angular power spectrum with at least 10 redshift slices [i.e. with $\Delta z \lesssim 0.1(1+z)$, where the data are binned also in photon counts] gives exceptional 1σ marginal error bars on the non-linearity parameter of $\Delta f_{\rm NL}^{\rm local} \lesssim 10$. This also provides tighter constraints than any number-count experiment in (photometric-) redshift bins for all cosmological parameters with the exception of $\Omega_{\rm m}$. The combination of one- and two-point statistics in tomographic slices based on photometric redshifts is optimal, with $\Delta f_{\rm NL}^{\rm local} \simeq 9$, $\Delta\sigma_8 \simeq 0.036$ (4.4 per cent) and $\Delta\Omega_{\rm m} \simeq 0.012$ (4.2 per cent) (see Table 3).

(iv) Also for the LM scaling relation, C_ℓ tomography gives tighter constraints than cluster number counts, although this result is reversed with a deeper exposure ($T_{\rm exp} = 3$ ks). The joint analysis of the two *eROSITA* experiments improves the current error bars on the slope of the LM relation by a factor of 3 (see Table 3).

(v) Measuring spectroscopic redshifts for the individual clusters would further tighten the marginal error on each parameter by an additional $\sim$30–40 per cent with respect to the photo-z case. This applies to all parameters but $f_{\rm NL}^{\rm local}$, which exhibits somewhat smaller improvements (see Table 5).

(vi) Yet, even the optimal combination of *eROSITA* measurements with redshift information only loosely constrains parameters such as $n_{\rm s}$, h and $\Omega_{\rm b}$. Standard priors on h and $\Omega_{\rm b}$ are necessary to reduce uncertainties for this subset of the parameter space (see Section 8.4).

(vii) If we could perfectly characterize the LM scaling relation with prior data, *eROSITA* (with photometric redshifts) would constrain the vanilla ΛCDM in line with the future CMB mission *Planck*, with unrivaled constraints on the amplitude of the linear DM power spectrum σ_8 (to 0.4 per cent accuracy; see Tables B1 and B2). In fact, while accounting for primordial non-Gaussianity does not sensibly degrade the best constraints on σ_8 and $\Omega_{\rm m}$, the LM relation is the main source of noise in the measurement of cosmological parameters out of the *eROSITA* cluster sample (see Table 3 versus Table B1).

(viii) In turn, combining *eROSITA* and *Planck* data gives sensational constraints on both the cosmology and the ICM sectors (see Table 3). Note that $\Delta f_{\rm NL}^{\rm local} \simeq 7$, $\Delta\sigma_8 = 0.014$ and $\Delta\Omega_{\rm m} = 0.0039$ as well as $\Delta\alpha_{\rm LM} = 0.02$ and $\Delta\gamma_{\rm LM} = 0.07$.

(ix) Other models of primordial non-Gaussianity are analysed in addition to the local shape: the best constraints (with no priors) read $\Delta f_{\rm NL} \simeq 9, 36$, and 144 for the local, orthogonal and equilateral shape, respectively, and 7, 19 and 115 when *Planck* priors are applied to the other cosmological parameters (see Table 6).

(x) Regarding the survey strategy, we find that the all-sky survey ($f_{\rm sky} = 0.658$, $T_{\rm exp} = 1.6$ ks) is the optimal choice with respect to a possible deeper and smaller survey ($f_{\rm sky} = 0.15$, $T_{\rm exp} = 7.5$ ks) in terms of parameter estimation (see Table 4).

(xi) All the results summarized above are obtained considering galaxy clusters with mass $M > 5 \times 10^{13}\,h^{-1}\,{\rm M}_\odot$ (in the fiducial model). Lowering this threshold would increase the constraining power of the experiments in the Fisher-matrix analysis. This formal improvement, however, would be achievable only if robust knowledge of the X-ray scaling relations at low masses were available, which nowadays is not the case.

(xii) The forecasted error estimates for the cosmological parameters are affected by the exact form and redshift evolution of the fiducial LM scaling relation. Switching from the observationally motivated relation by Vikhlinin et al. (2009a) (our reference choice) to the one by Mantz et al. (2010a) shrinks the forecasted errors by a factor ranging between 10 and 50 per cent, except for $f_{\rm NL}^{\rm local}$ and $\Omega_{\rm m}$ (whose constraints are barely affected, see Section 11.2). This shows that our main results might possibly be conservative.

(xiii) It is impossible to constrain the temperature–mass scaling relation on top of our standard 10 parameters (Section 11.3).

(xiv) The Limber approximation for the calculation of the angular power spectrum is less accurate in the presence of a scale-dependent halo bias induced by primordial non-Gaussianity than previously established using Gaussian initial conditions. The erroneous use of the Limber approximation on large angular scales would optimistically underestimate the marginal constraints on $f_{\rm NL}^{\rm local}$ by a factor of 4.

In conclusion, together with the *Planck* satellite and upcoming photometric galaxy surveys, *eROSITA* will substantially contribute to the simultaneous determination of the cosmological parameters and of the X-ray luminosity–mass relation. In particular, it will shed new light on the physics of the primordial universe by constraining the non-linearity parameter with remarkable accuracy, and possibly rule out entire classes of inflationary models. Further studies will focus on the design of dedicated follow-up campaigns to further exploit the *eROSITA* cluster sample.

ACKNOWLEDGMENTS

We thank Peter Kalberla for providing Galactic hydrogen data tables from the LAB survey, Frank Haberl for *eROSITA* response matrices, and Jan Robrade for *eROSITA* exposure maps. We express our gratitude to Alexey Vikhlinin for providing the luminosity–mass relation expression with the mass pivot, to Dragan Huterer and Wayne Hu for kindly providing the *Planck* priors, to Jeremy Tinker for the mass function parameter covariance matrices, and to Andres Balaguera Antolinez for carefully reading the manuscript. AP thanks Julien Carron for the amusing and useful conversations about Fisher matrices and Tommaso Giannantonio for many detailed exchanges. AP acknowledges support from the Swiss Science National Foundation. CP and THR acknowledge support from the German Research Association (DFG) through the Transregional Collaborative Research Center 'The Dark Universe' (TRR33) and (for THR) through Heisenberg grants RE 1462/5 and RE 1462/6. *eROSITA* is funded equally by the DLR and the Max-Planck-Gesellschaft zur Förderung der Wissenschaften (MPG).

REFERENCES

Albrecht A. et al., 2006, preprint (astro-ph/0609591)
Albrecht A. et al., 2009, preprint (arXiv:0901.0721)
Allen S. W., Evrard A. E., Mantz A. B., 2011, ARA&A, 49, 409
Anders E., Grevesse N., 1989, Geochim. Cosmochim. Acta, 53, 197
Arnaud K. A., 1996, in Jacoby G. H., Barnes J., eds, ASP Conf. Ser. Vol. 101, Astronomical Data Analysis Software and Systems V. Astron. Soc. Pac., San Francisco, p. 17
Babich D., Creminelli P., Zaldarriaga M., 2004, J. Cosmol. Astropart. Phys., 08, 009

Baldauf T., Seljak U., Senatore L., Zaldarriaga M., 2011, J. Cosmol. Astropart. Phys., 10, 031
Bartolo N., Komatsu E., Matarrese S., Riotto A., 2004, Phys. Rep., 402, 103
Bertschinger E., 2001, ApJS, 137, 1
Catelan P., Lucchin F., Matarrese S., Porciani C., 1998, MNRAS, 297, 692
Chen X., 2010, Advances Astron., 2010, 72
Cohn J. D., 2006, New Astron., 11, 226
Cole S., Kaiser N., 1989, MNRAS, 237, 1127
Creminelli P., Nicolis A., Senatore L., Tegmark M., Zaldarriaga M., 2006, J. Cosmol. Astropart. Phys., 05, 004
Cui W., Borgani S., Dolag K., Murante G., Tornatore L., 2011, preprint (arXiv:1111.3066)
Cunha C. E., Evrard A. E., 2010, Phys. Rev. D, 81, 83509
Cunha C., Huterer D., Doré O., 2010, Phys. Rev. D, 82, 23004
Dalal N., Doré O., Huterer D., Shirokov A., 2008, Phys. Rev. D, 77, 123514
Davis M., Efstathiou G., Frenk C. S., White S. D. M., 1985, ApJ, 292, 371
Desjacques V., Seljak U., 2010, Classical Quantum Gravity, 27, 4011
Desjacques V., Seljak U., Iliev I. T., 2009, MNRAS, 396, 85
Desjacques V., Jeong D., Schmidt F., 2011, Phys. Rev. D, 84, 63512
Eckmiller H. J., Hudson D. S., Reiprich T. H., 2011, A&A, in press (arXiv:1109.6498)
Efstathiou G., Davis M., White S. D. M., Frenk C. S., 1985, ApJS, 57, 241
Einasto J., Klypin A. A., Saar E., Shandarin S. F., 1984, MNRAS, 206, 529
Fedeli C., Moscardini L., Matarrese S., 2009, MNRAS, 397, 1125
Fedeli C., Carbone C., Moscardini L., Cimatti A., 2011, MNRAS, 414, 1545
Freedman W. L. et al., 2001, ApJ, 553, 47
Giannantonio T., Porciani C., 2010, Phys. Rev. D, 81, 63530
Giannantonio T., Porciani C., Carron J., Amara A., Pillepich A., 2011, MNRAS, in press (arXiv:1109.958)
Hu W., 2003, Phys. Rev. D, 67, 81304
Hu W., Jain B., 2004, Phys. Rev. D, 70, 43009
Hu W., Kravtsov A. V., 2003, ApJ, 584, 702
Huterer D., Takada M., Bernstein G., Jain B., 2006, MNRAS, 366, 101
Kalberla P. M. W., Burton W. B., Hartmann D., Arnal E. M., Bajaja E., Morras R., Pöppel W. G. L., 2005, A&A, 440, 775
Khedekar S., Majumdar S., Das S., 2010, Phys. Rev. D, 82, 41301
Kirkman D., Tytler D., Suzuki N., O'Meara J. M., Lubin D., 2003, ApJS, 149, 1
Komatsu E. et al., 2009, ApJS, 180, 330
Komatsu E. et al., 2011, ApJS, 192, 18
Kravtsov A. V., Vikhlinin A., Nagai D., 2006, ApJ, 650, 128
Lima M., Hu W., 2004, Phys. Rev. D, 70, 43504
Loverde M., Afshordi N., 2008, Phys. Rev. D, 78, 123506
LoVerde M. L., Miller A., Shandera S., Verde L., 2008, J. Cosmol. Astropart. Phys., 04, 014
Majumdar S., Mohr J. J., 2003, ApJ, 585, 603
Manera M., Sheth R. K., Scoccimarro R., 2010, MNRAS, 402, 589
Mantz A., Allen S. W., Ebeling H., Rapetti D., Drlica-Wagner A., 2010a, MNRAS, 406, 1773
Mantz A., Allen S. W., Rapetti D., Ebeling H., 2010b, MNRAS, 406, 1759,
Mittal R., Hicks A., Reiprich T. H., Jaritz V., 2011, A&A, 532, 133
Mo H. J., White S. D. M., 1996, MNRAS, 282, 347
More S., Kravtsov A. V., Dalal N., Gottlöber S., 2011, ApJS, 195, 4
Oguri M., 2009, Phys. Rev. Lett., 102, 211301
Pillepich A., Porciani C., Hahn O., 2010, MNRAS, 402, 191
Pratt G. W., Croston J. H., Arnaud M., Böhringer H., 2009, A&A, 498, 361
Predehl P., 2006, in Turner M. J. L., Hasinger G., eds, SPIE 6266, Space Telescopes and Instrumentation II. SPIE, Bellingham, p. 62660P-10
Predehl P. et al., 2010, preprint (arXiv:1001.2502)
Roncarelli M., Moscardini L., Branchini E., Dolag K., Grossi M., Iannuzzi F., Matarrese S., 2010, MNRAS, 402, 923
Sartoris B., Borgani S., Fedeli C., Matarrese S., Moscardini L., Rosati P., Weller J., 2010, MNRAS, 407, 2339
Schmidt F., Kamionkowski M., 2010, Phys. Rev. D, 82, 103002
Schuecker P. et al., 2001, A&A, 368, 86
Senatore L., Smith K. M., Zaldarriaga M., 2010, J. Cosmol. Astropart. Phys., 01, 028
Shaw L. D., Holder G. P., Dudley J., 2010, ApJ, 716, 281
Simon P., 2007, A&A, 473, 711
Smith R. K., Brickhouse N. S., Liedahl D. A., Raymond J. C., 2001, ApJ, 556, L91
Smith R. E., Scoccimarro R., Sheth R. K., 2007, Phys. Rev. D, 75, 63512
Stanek R., Rudd D., Evrard A. E., 2009, MNRAS, 394, L11
Stanek R., Rasia E., Evrard A. E., Pearce F., Gazzola L., 2010, ApJ, 715, 1508
Sun M., Voit G. M., Donahue M., Jones C., Forman W., Vikhlinin A., 2009, ApJ, 693, 1142
Takada M., Bridle S., 2007, New J. Phys., 9, 446
Taruya A., Koyama K., Matsubara T., 2008, Phys. Rev. D, 78, 123534
Tegmark M., Taylor A. N., Heavens A. F., 1997, ApJ, 480, 480, 22
Tinker J., Kravtsov A. V., Klypin A., Abazajian K., Warren M., Yepes G., Gottlöber S., Holz D. E., 2008, ApJ, 688, 709
Tinker J. L., Robertson B. E., Kravtsov A. V., Klypin A., Warren M. S., Yepes G., Gottlöber S., 2010, ApJ, 724, 878
Tozzi P., Rosati P., Ettori S., Borgani S., Mainieri V., Norman C., 2003, ApJ, 593, 705
Vikhlinin A. et al., 2009a, ApJ, 692, 1033
Vikhlinin A. et al., 2009b, ApJ, 692, 1060
Wands D., Slosar A., 2009, Phys. Rev. D, 79, 123507
Wu H.-Y., Zentner A. R., Wechsler R. H., 2010, ApJ, 713, 856
Yamamoto K., Parkinson D., Hamana T., Nichol R. C., Suto Y., 2007, Phys. Rev. D, 76, 129901
Yoo J., 2010, Phys. Rev. D, 82, 83508

APPENDIX A: ERROR ELLIPSES

We show here the joint (marginal) 1σ error ellipses for all the parameter pairs of our main analysis. Results from different experiments are colour-coded as in Fig. 11, but differently from there results are given adopting the external priors on h and $\Omega_{\rm b}$, as detailed in Section 8.4. Note that the contours obtained from the number-count experiment with no redshift information exceed the area in the plot in all cases but for the pair $\Omega_{\rm b}$ and h, where they are indistinguishable from the results of the number counts with photometric redshifts.

APPENDIX B: ADDITIONAL RESULTS

We report here some additional results which may still be of interest for the community and shall facilitate comparisons with analogue calculations in the literature. First of all, we show in Table B1 the *eROSITA* constraints on the cosmological parameters that would be obtained if the four parameters in the LM relation were perfectly known before performing the observations (six-parameter fit). These are the most optimistic constraints that can be achieved using *eROSITA* data. Comparing these results with Table 3 shows a manifest degradation of the results due to the inclusion of the four additional LM parameters: marginal errors on σ_8 and $\Omega_{\rm m}$ are tighter by a factor of 10 when the ICM parameters are kept fixed. This suggests that extracting cluster subsamples for which precise determinations of the observable–mass relation could be obtained will be a convenient strategy.

In order to assess the impact of adding $f_{\rm NL}^{\rm local}$ to the set of free parameters, in Table B2 we repeat the analysis by assuming that both the LM relation and $f_{\rm NL}^{\rm local}$ are perfectly known in advance (five-parameter fit). This shows that accounting for primordial non-Gaussianity of the local type does not sensibly degrade the constraints on the ΛCDM parameters, although details depend somewhat on the individual experiments which are considered. Table B2 shows a comparison between *eROSITA* and *Planck*, if LM and $f_{\rm NL}^{\rm local}$ parameters were perfectly known and where cosmological results for *Planck* come from a five-parameter fit of the power spectrum

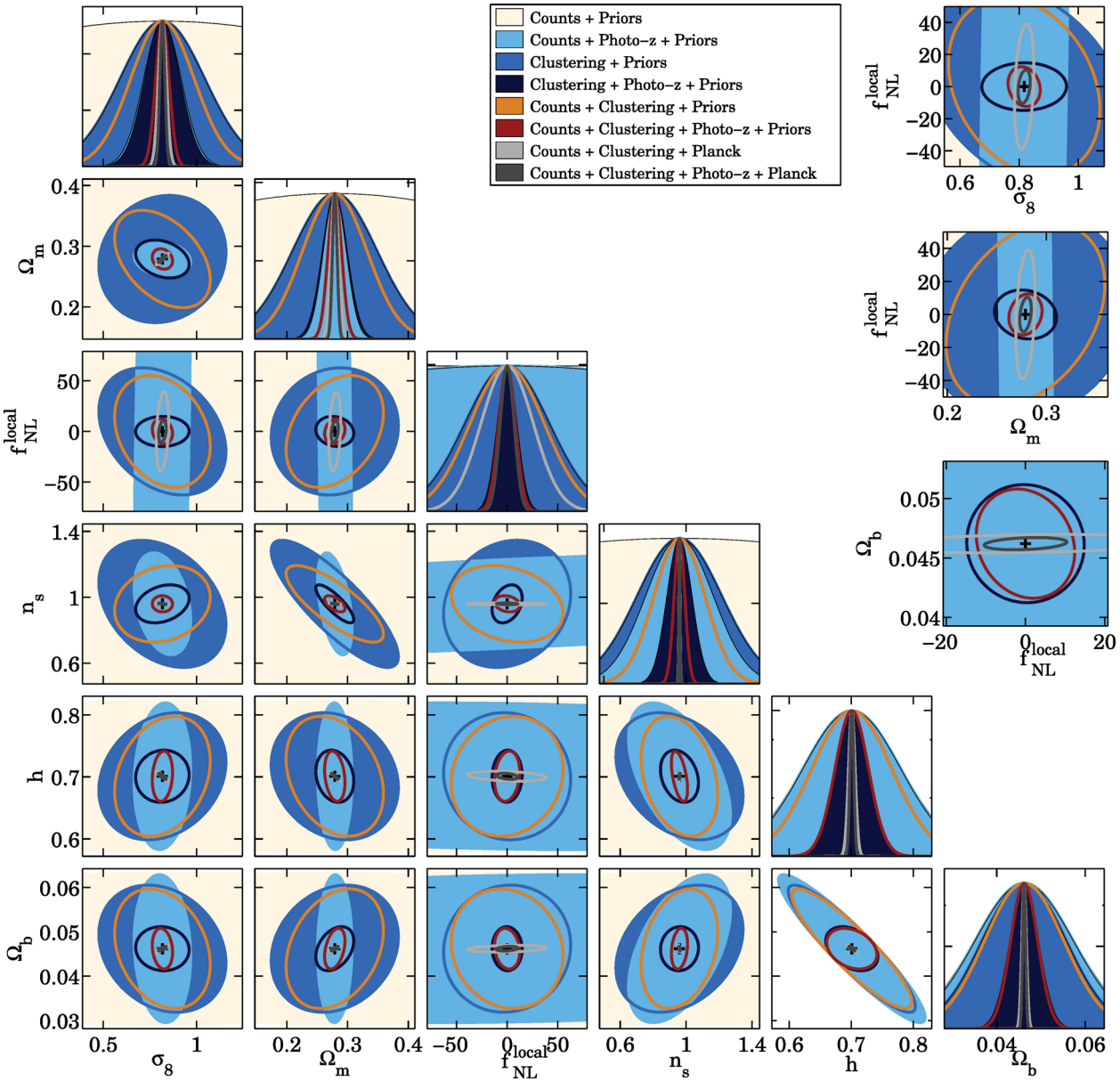

Figure A1. Joint 1σ error ellipses for the cosmology sector. Colour coding is as in Fig. 11. The three top-right panels are zoomed-in version of the corresponding panels in the matrix.

of the temperature anisotropies, for Gaussian initial conditions. Finally, in Table B3 we show how increasing the number of free parameters in the fit to the data degrades the marginal constraints on σ_8 from the *eROSITA* cluster number counts. In this exercise, the parameters which are not fitted are assumed to be perfectly known. No prior knowledge of any sort is instead considered for the fitted parameters. It is worthwhile mentioning that adding the four parameters of the TM relation to our 'cosmology-only' six-parameter fit gives a marginal error on σ_8 which is three times smaller than what is obtained by adding the four parameters regulating the LM relation and its redshift evolution. This occurs also for all the other cosmological parameters, although at lower extents. Once again this shows that some knowledge of the LM relation is the most important piece of information on the ICM physics which is necessary to accurately determine the cosmological parameters. This holds true also for the measurements of the angular power spectrum.

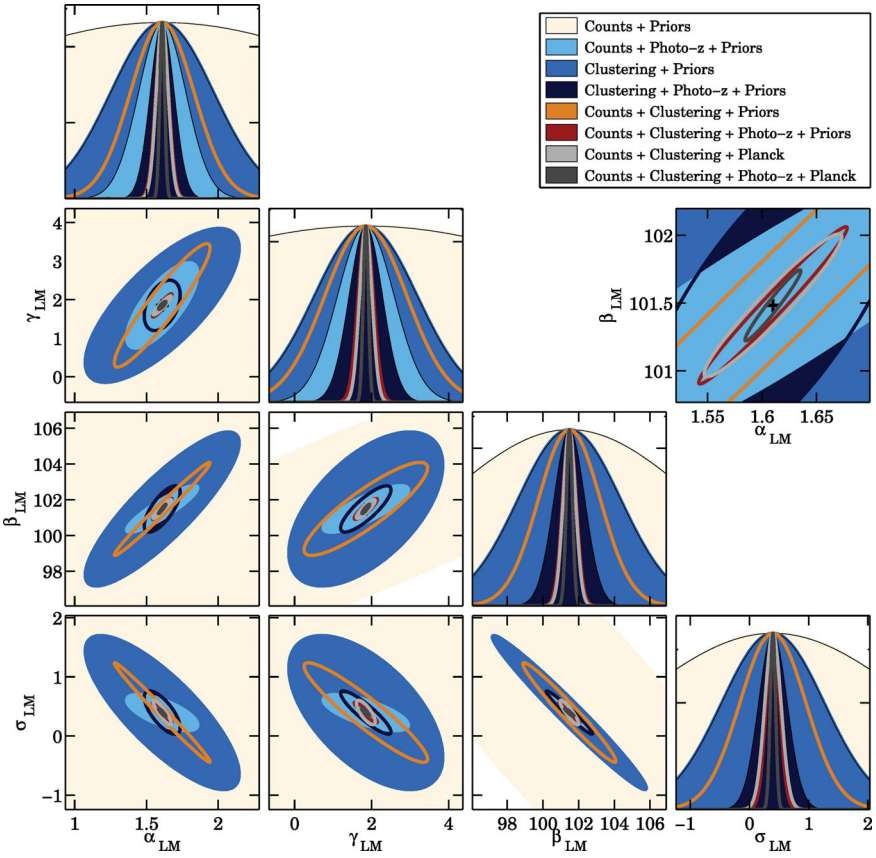

Figure A2. As in Fig. A1 but for the parameters of the LM scaling relation. The top-right panel is a zoomed-in version of the corresponding panel in the matrix.

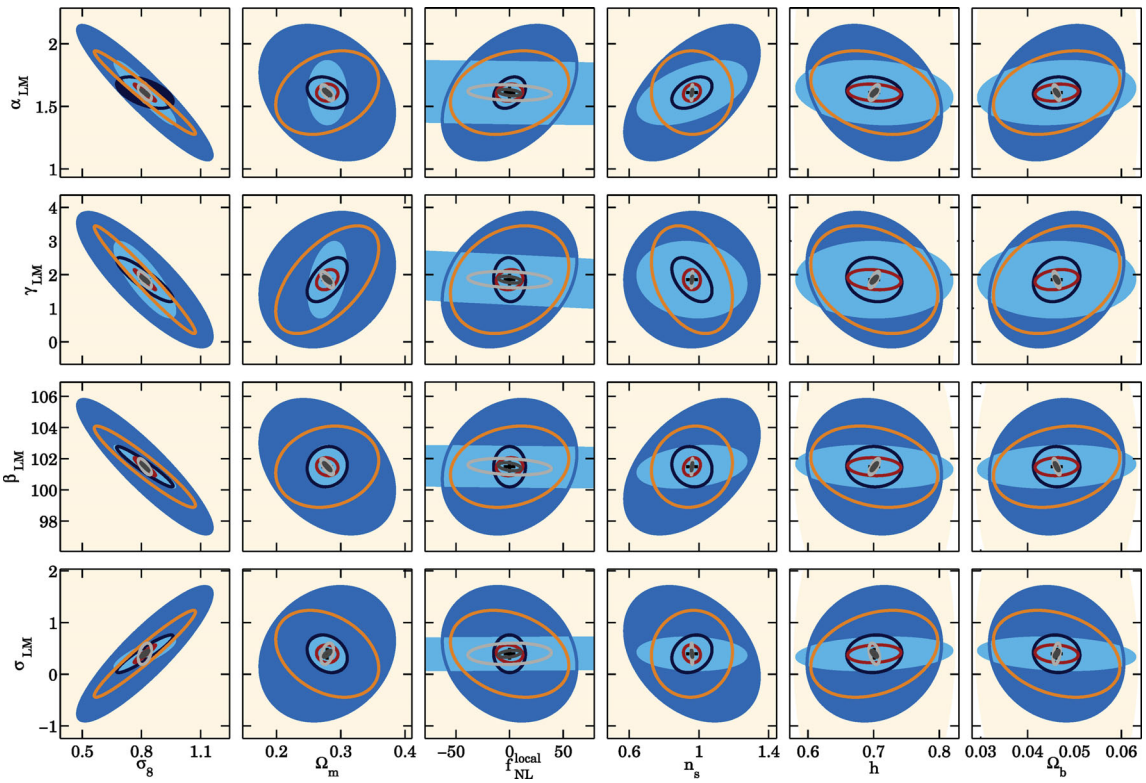

Figure A3. As in Fig. A1 but for pairs of parameters belonging to different sectors.

Table B1. As in Table 3 with no priors but marginalizing only over the cosmological sector, fixing the ICM parameters.

eROSITA data	FoM	$\Delta f_{\rm NL}^{\rm local}$	$\Delta\sigma_8$	$\Delta\Omega_{\rm m}$	$\Delta n_{\rm s}$	Δh	$\Delta\Omega_{\rm b}$
Counts	2.7	$\sim 7 \times 10^3$	0.804	0.2725	$\sim$1	$\sim$2	$\sim$0.2
Counts + Photo-z	8.2	85	0.017	0.0086	0.172	0.371	0.0514
Angular clustering	6.1	43	0.028	0.0241	0.467	$\sim$1	0.0797
Angular clustering + Photo-z	8.8	9.3	0.016	0.0101	0.084	0.151	0.0113
Counts + Angular clustering	8.0	36	0.016	0.0099	0.172	0.461	0.0464
Counts + Angular clustering + Photo-z	11.0	8.4	0.003	0.0029	0.055	0.110	0.0092
Current errors	–	[−10,+74]	0.024	0.0061	0.012	0.014	0.0016
Planck errors	–	–	0.024	0.0071	0.004	0.006	0.0006

Table B2. As in Table 3 with no priors unless explicitly stated but marginalizing only over five parameters of the cosmological sector, fixing both the ICM parameters and $f_{\rm NL}^{\rm local} \equiv 0$.

eROSITA data	FoM	$\Delta\sigma_8$	$\Delta\Omega_{\rm m}$	$\Delta n_{\rm s}$	Δh	$\Delta\Omega_{\rm b}$
Counts	6.5	0.196	0.1213	$\sim$1	$\sim$2	$\sim$0.2
Counts + Photo-z	10.1	0.003	0.0031	0.143	0.364	0.0492
Angular clustering	7.7	0.025	0.0228	0.369	0.783	0.0688
Angular clustering + Photo-z	9.8	0.015	0.0100	0.078	0.138	0.0107
Counts + Angular clustering	9.5	0.015	0.0094	0.156	0.439	0.0459
Counts + Angular clustering + Photo-z	11.9	0.003	0.0027	0.050	0.104	0.0090
Counts + Angular clustering + *Planck*	16.1	0.002	0.0010	0.002	0.001	0.0002
Counts + Angular clustering + Photo-z + *Planck*	16.3	0.001	0.0008	0.002	0.001	0.0002
Current errors	–	0.024	0.0061	0.012	0.014	0.0016
Planck errors	14.3	0.024	0.0071	0.004	0.006	0.0006

Table B3. The marginal error on σ_8 as determined from the number-count experiment with photometric redshifts is shown as a function of the number of free parameters used to fit the *eROSITA* data. The last column lists the parameter showing the largest linear correlation coefficient with σ_8. Note that LM and TM stand respectively for the luminosity–mass relation and the temperature-mass relation. The row in boldface indicates the reference set-up adopted throughout this work.

Parameter set	# parameters	$\Delta\sigma_8$ ($\Delta\sigma_8/\sigma_8$)	Most correlated parameter
σ_8	1	0.0005 (0.06 per cent)	–
$\sigma_8 + \Omega_{\rm m} + n_{\rm s} + h + \Omega_{\rm b} = \Lambda$CDM	5	0.003 (0.4 per cent)	$\Omega_{\rm m}$
ΛCDM + $f_{\rm NL}^{\rm local}$	6	0.017 (2.1 per cent)	$\Omega_{\rm m}, f_{\rm NL}^{\rm local}$
ΛCDM + LM sector	9	0.113 (14 per cent)	$\gamma_{\rm LM}$
ΛCDM + $f_{\rm NL}^{\rm local}$ + LM sector	**10**	**0.113 (14 per cent)**	$\boldsymbol{\beta_{\rm LM}}$
ΛCDM + $f_{\rm NL}^{\rm local}$ + TM sector	10	0.038 (4.6 per cent)	$\Omega_{\rm m}$
ΛCDM + $f_{\rm NL}^{\rm local}$ + LM sector + TM sector	14	0.192 (23 per cent)	$\beta_{\rm LM}$

This paper has been typeset from a TEX/LATEX file prepared by the author.